UTRECHT UNIVERSITY

MASTER THESIS

Transport and Variability of the Irminger Current between 2014 and 2015

Author:
Stylianos Kritsotalakis

Supervisors:
Prof. Dr. Sybren Drijfhout
Dr. Laura de Steur

A thesis submitted in fulfillment of the requirements for the degree of Master in Meteorology, Physical Oceanography and Climate

in the

Institute for Marine and Atmospheric Reasearch (IMAU)

December 1, 2016

Universiteit Utrecht

"The unstable ocean" - by Ntina Karakosta

"Hofstadter's Law: it always takes longer than you expect, even when you take into account Hofstadter's Law. ."

Douglas Hofstadter

Aknoledgements

I am grateful to Laura de Steur for a handful of reasons. First, she offered me the unique opportunity to take part in the scientific cruise that introduced me to the world of observational physical oceanography. Then, when I knocked her door asking for more data she willingly introduced me to this topic. She guided my way through this project in various ways and challenged me to tackle the problems I faced. During my stay at NIOZ, interaction with experienced researchers improved my understanding of the ocean dynamics and my academic skills. Femke de Jong helped me to develop better insight into my study topic through numerous discussions, suggestions and critical comments. Leandro Ponsoni and Borja Aguiar Gonzalez, supported my research with their interest and valuable input.I want to thank Sybren Drijfhout, my supervisor at Utrecht University, for his feedback and challenging remarks during our meetings. Lastly, I want to thank my family, my friends and Dimitra for their unconditional support during my studies.

Utrecht University

Abstract

Institute for Marine and Atmospheric Reasearch (IMAU)

Master in Meteorology, Physical Oceanography and Climate

Transport and Variability of the Irminger Current between 2014 and 2015

by Stylianos KRITSOTALAKIS

The Irminger Current, a branch of the North Atlantic Current, carries warm and saline waters poleward in the subpolar gyre and as such contributes to the upper limb of the Atlantic Meridional Overturning Circulation (AMOC). Previous estimates about its volume transport and variability have been mostly based on summer hydrographic sections in combination with satellite data. Presented here are the first year-round results from a full-depth mooring array located on the west side of the Reykjanes Ridge between 2014 and 2015. These results are mainly compared with hydrographic and velocity data from summers 2014 and 2015 and shipboard measurements from the early 1990s and 2000s, where the shift in atmospheric forcing resembles that of winter 2014-2015. Differences in the shape and strength of the Irminger Current are large during this one-year period. The IC is highly variable on scales varying from 7 to 35 days. Changes in the velocity field during the winter state are distinct and occur concurrently with record deep convection in the Irminger Gyre. The spatial resolution of the moorings is found to be likely too coarse to capture the full transport of the Irminger Current. Additional data from oceanic moorings from a French campaign will help to resolve this in the future. These first year-round results show that the Irminger Current is much more variable than earlier thought, particularly during winter.

Contents

Chapter 1 - Introduction . . . 1
1.1. Circulation in the Subpolar North Atlantic . . . 1
1.2. The Irminger Sea . . . 2
1.3. Atmospheric forcing and convection . . . 3
1.4. Motivation for this study . . . 4
Chapter 2 - Hydrographic and circulation changes between summer 2014 and 2015 5
2.1. Data and methods . . . 5
2.1.1. Hydrographic observations from the Irminger Basin . . . 7
2.1.2. Direct velocity observations from the Irminger basin . . . 7
2.2. Results: Atmospheric forcing during the winter of 2014-2015 . . . 9
2.3. Results: Evidence of convective activity . . . 10
2.4. Results: Changes in the circulation . . . 13
2.4.1. Absolute geostrophic velocities . . . 13
2.4.2. Geostrophic Volume Transport . . . 14
Chapter 3 - Variability of the Irminger Current . . . 16
3.1. Data and methods . . . 16
3.1.1. Mooring data from the Irminger Current . . . 16
3.1.1.1. Treatment of velocity (ADCP, CM) measurements . . . 16
3.1.1.2. Treatment of MCTD measurements . . . 19
3.1.1.3. Gridding . . . 19
3.2. Results: Directional Preference . . . 23
3.3. Results: Spectral analysis of across-section velocities . . . 25
3.4. Results: Monthly and seasonal changes . . . 27
3.4.1. Changes in stratification and eddy activity . . . 27
3.4.2. Monthly changes in conservative temperature . . . 29
3.4.3. Monthly changes in across-section velocities . . . 30
3.4.4. Seasonal changes . . . 31
Chapter 4 - Results: Volume Transport . . . 33
4.1. Total net volume transport . . . 33
4.2. Volume Transport of the Irminger Current . . . 36
4.3. Comparison of northward volume transport estimates . . . 37
Chapter 5 - Results: Mean Absolute Dynamic Topography . . . 39
Chapter 6 - Conclusions and recommendations . . . 43
6.1. Summary and conclusions . . . 43
6.2. Recommendations for further study . . . 44
Appendix: Extra figures . . . 48
Music from time series . . . 48

Chapter 1 - Introduction

1.1. Circulation in the Subpolar North Atlantic

Ocean circulation in the subpolar North Atlantic, as a part of the Atlantic Meridional Overturning Circulation (AMOC), constitutes a key component of the global thermohaline circulation driven by heat and salt. Its variability strongly affects weather and climate in Europe (Rhein et al., 2011). The pathways and the strength of the currents in the subpolar North Atlantic have an important and direct effect in this thermohaline circulation. The North Atlantic Current (NAC) is the northeastward extension of the Gulf stream and carries warm and saline upper-ocean waters from the subtropics poleward. Across the mid-Atlantic Ridge, the NAC splits into two major branches. One branch flows northeastwards towards the Nordic seas after its passage between Iceland and Scotland. The other one circulates cyclonically around the Icelandic basin, loops around the Reykjanes Ridge (RR) and enters the Irminger basin as a northward flow. This northward flow forms the Irminger Current which also circulates cyclonically around the Irminger basin (e.g. Flatau et al., 2003; Pickart et al., 2005). On the east coast of Greenland, the IC forms the upper part of the Western Boundary Current (WBC) together with the East Greenland Current (EGC) which transports cold and fresh waters advected from the Greenland Sea (e.g., Lherminier et al., 2007; Sarafanov et al., 2012). The circulation closes with the West Greenland Current (WGC) in the Labrador Sea that feeds the southward-flowing Labrador Current off the coast of Canada.

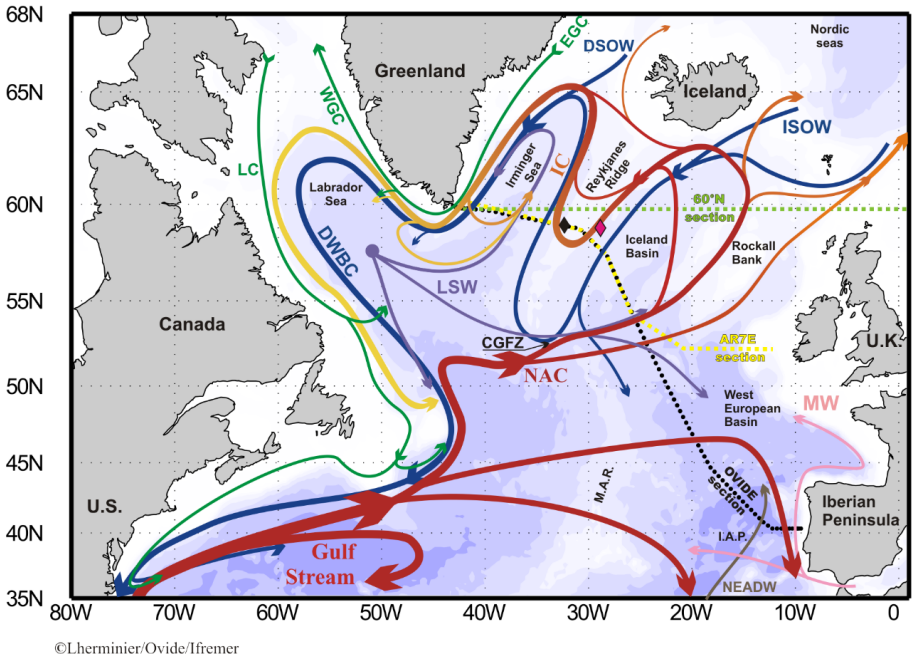

FIGURE 1: Schematic illustration of the warm and salty (red and orange) and cold and fresh (blue and green) currents in the North Atlantic Ocean. An overview of the circulation can also be found in Daniault et al., 2006.

The above closed upper-ocean cyclonic circulation, lies roughly between 45°N and 65°N in the subpolar North Atlantic and is called the Subpolar Gyre (SPG). In this area, densification of surface waters occurs via loss of heat to the atmosphere and deep convection (during wintertime) occurs in the central part of the basins (Labrador and Irminger). These waters also mix with the inflow of cold freshwater from the Arctic and ultimately sink to accomplish a roundtrip to the subtropics as cold and fresh deep ocean waters. The dynamics of the boundary-currents play an important role in the restratification of the interior and hence in the rate of deep water formation (Katsman et al.,2004). Finally, The SPG serves as a pathway of atmospheric carbon dioxide into the deep ocean (e.g. Corbiere et al., 2007; Halloran et al., 2015).

1.2. The Irminger Sea

The area of interest here, is the Irminger Sea (IS) which is located between southeast Greenland and the mid-Atlantic Ridge and comprises a transition area between warm and saline Atlantic origin waters and cold and fresh ones of Arctic origin. Although the general circulation of the Irminger Sea is fairly well known, important characteristics of the boundary currents on both sides of the basin, and their role in the interior flow, are not well known.

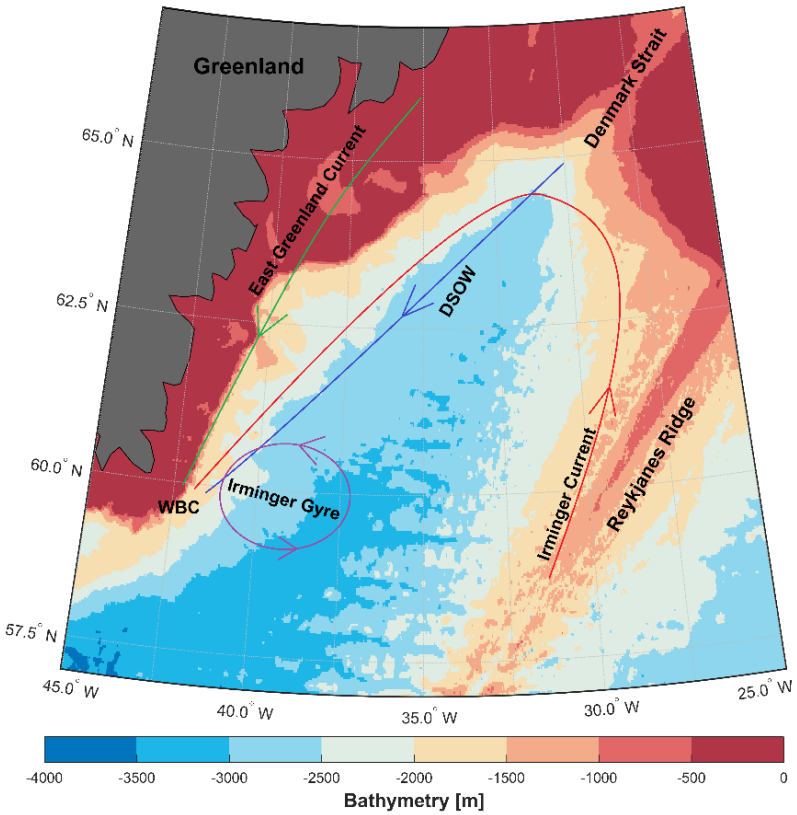

FIGURE 2: Schematic Illustration of the main circulation features in the Irminger Sea. The Irminger and the East Greenland surface currents are illustrated with red (warm and saline waters) and green (cold and fresh waters) respectively. They combine to form the Western Boundary Current (WBC) in the basin. The Denmark Straight Overflow Water (DSOW) that contributes to the deep part of the WBC is shown with blue color. The Irminger Gyre is marked with purple.

On the eastern side of the Irminger basin adjacent to the Reykjanes Ridge, the surface NAC enters the area as the Irminger Current (IC) and circulates cyclonically around the Irminger Sea. On the western side of the basin in the vicinity of Cape Farewell, Atlantic and Artic water masses combine to shape the Western Boundary Current (WBC). This southwestward flow extends all the way to the bottom off the ocean, along the shelf and continental slope of Greenland. Another feature located on the southwestern side of IS, is the Irminger Gyre (IG). It is a narrow cyclonic recirculation, part of a band of low geostrophic pressure shared among the Irminger and Labrador Seas (Lavender et al., 2000). It is mostly a barotropic feature and short in geostrophic shear and as a consequence it is difficult to be detected in hydrographic data. Moreover, wintertime convection favors the formation of Labrador Sea Water (LSW) inside this gyre (Pickart et al., 2003). LSW is an intermediate water mass that is primarily formed in the neighboring Labrador Sea (Lazier et al.,2002) and being advected to the Irminger Sea. The deep part of the ocean in the Irminger Sea is occupied by the Denmark Strait and the Iceland-Scotland overflow waters. These waters originate from the Nordic Seas, cascade downstream of sills and spread into the open ocean to form the deep part of the WBC. Like in other basins in the North Atlantic (e.g. Labrador basin), the Irminger Sea is an area of intense eddy activity. Eddies in the Irminger basin have been observed in many studies (e.g. Holiday et al., 2007; Våge et al.,2011; de Jong et al.,2011) but not extensively analyzed. Accurate description of these different currents and physical processes that take place in the Irminger Sea and their interconnection, will ultimately lead to a more complete understanding of the role of the Irminger Sea in the climate system of the North Atlantic.

1.3. Atmospheric forcing and convection

The Irminger Sea is located below the North Atlantic storm track and consequently comprises an area of intense air-sea interaction. The number and strength of these low-pressure systems that pass through the Irminger Sea, is influenced by the state of the North Atlantic Oscillation (NAO). The NAO is characterized: a) by an index (NAO index) which is based on the difference in the local sea level pressure between the low and high pressure systems, above Iceland and Azores respectively, or b) by the first empirical orthogonal function (EOF) of the mean sea level pressure over the same locations. This pressure dipole is of course not fixed in space and time. Instead, its position and strength varies over a period of months (or even years) which brakes the assumption of orthogonality and symmetry. To tackle this problem, other frameworks that try to explain the atmospheric forcing of the North Atlantic Ocean circulation are being investigated (e.g. Barrier et al.,2013). However, the NAO is responsible for a large fraction of the interannual and interdecadal variability in the North Atlantic. NAO possesses a positive (strong pressure dipole and westerly winds) and a negative (weak pressure dipole and westerly winds) phase that modulate the strength and direction of both the westerly winds and the storm tracks across the vast North Atlantic. While in a positive state, the Irminger Sea experiences stronger westerly winds, more and stronger cyclones and a northeastward shift in the storm track (e.g. Rogers,1990). Nevertheless, the high topography of Greenland controls the local air-sea interaction. In the southeastern tip of Greenland, phenomena known as tip jets are initiated with the passage of cyclones to the northeast (e.g. Doyle and Shapiro, 1999).

These tip jets are spatially limited but powerful wind events that are linked with the oceanic circulation in the inner Irminger Sea. They are correlated with greater than normal wind stress curl which in turn induces upwelling in the cyclonically rotating Irminger Gyre (Pickart et al.,2003).

Extensive cooling of surface waters in a closed cyclonic circulation area, like the IG, favors deep convection - deep mixing of water particles due to instabilities of the water column. This area of cyclonic circulation is characterized by upward doming isopycnals which bring denser waters closer to the surface of the ocean. With the right preconditioning (upwelling) and sufficient buoyancy loss, stratification close to the surface collapses, the water column becomes unstable and overturns in the form of convective "chimneys". These dense waters sink and spread laterally through the basin. When the buoyancy loss to the atmosphere ceases, mixing stops and the process of restratification is initiated in the area. Mixed waters form smaller eddies, due to baroclinic instabilities, and less dense waters are allowed to enter the convective region.

1.4. Motivation for this study

The Irminger Current (IC) has not been extensively studied in the past. Little is known about the velocity structure, the transport and the variability of this current. The most thorough investigation thus far was presented in Våge et al.,2011. He used summer hydrographic data from 36 transects across the WOCE AR7E section for the period between 1991 to 2007. He distinguished two particularly interesting periods in terms of atmospheric forcing in the Irminger Sea: a) the 1990s (1990-1994), characterized by high atmospheric forcing (high NAO index), and b) the 2000s (2000-2004), characterized by low atmospheric forcing (low NAO index). He found that the shallow part of the IC (σ_θ < 27.70 kg m^{-3})) weakened between these two periods, but that during 2000s it developed a second, deep extension. Moreover, he noted that during this transition the mean full depth transport of the IC increased from 11 Sv in the 1990s to 14 Sv in the 2000s. Finally, he defined the IC as a 200km wide flow extending down to 1500m, approximately 500-700km off the coast of Greenland. Other estimates of the IC transport exist (e.g. 12 Sv mean 2002-2008 transport; Sarafanov et al., 2012) but these studies were not as extensive as the one conducted by Våge. In our study, we analyzed the first year-round data from a full-depth mooring array (west of the Reykjanes Ridge), that was placed in accordance with the findings of Våge et al.,2011. These data provide a first estimate of the year-round transport and the variability of the Irminger Current. This array is part of an international collaborative effort called Overturning of the Subpolar North Atlantic (OSNAP). OSNAP includes various mooring arrays across the North Atlantic and aims to get a better understanding of the complex North Atlantic circulation system. Additionally, through this study we aim to deliver valuable suggestions for future studies on the topic.

Chapter 2 - Hydrographic and circulation changes between summer 2014 and 2015

High atmospheric forcing (high NAO index) in the Irminger Sea can induce intense air-sea interaction and lead to anomalously large heat loss from the ocean to the atmosphere. These conditions could potentially trigger convection events in the Irminger Gyre and affect the circulation in the basin. Here, we illustrate the atmospheric conditions during the winter of 2014-2015 and present the results from the hydrographic sections taken across the basin in July 2014 and July 2015.

2.1. Data and methods

Hydrographic and direct velocity data used for this Chapter originate from two summer cruises in the Irminger sea carried out under the OSNAP program. Field campaigns were carried out between June^{25th} and July^{3rd}, 2014 by the royal research ship James Clark Ross and between July^{8th} and July^{29th}, 2015 by the research vessel Pelagia.

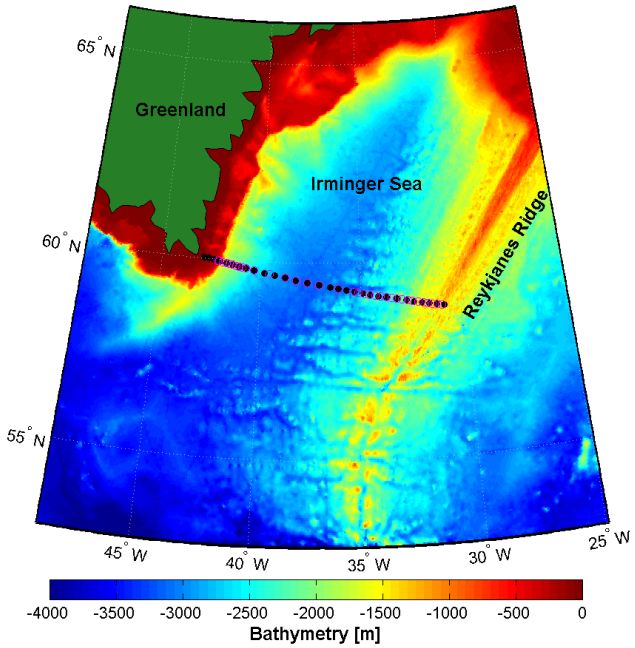

FIGURE 3: Bathymetry of the Irminger Sea derived from Etopo2v2 2-minute elevation database. Circles filled with black and magenta color represent CTD/LADCP measurement stations from 2014 and 2015 respectively.Greenland is illustrated with green color.

Both cruises crossed the Irminger sea, spanning a line, from the southern tip of Greenland to the west of the Reykjanes Ridge. Although most of the measurement stations overlap in space, coverage was denser in the middle of the basin in the first year and the west and east side in the following one. Additionally, during the summer of 2015 R/V Pelagia was blocked by sea ice ~ 50 km off the coast of Greenland and hence measurements were not conducted as west as in 2014. As a result, the total number of stations was 32 for the summer of 2014 and 35 for the summer of 2015 (Figure 3).

In order to illustrate differences between those two periods a procedure similar to Sarafanov et.al, (2012) was applied to the data. Initially a Least-Squares Regression line (LSR) was fit through the locations of the hydrographic stations which were then orthogonally projected to this line, while keeping individual-station bathymetry intact. This was possible because a) the discrepancy between the stations' original and projected position was mostly <1% while only once reached 5% and b) the standard deviation of the residuals of the LSR was 0.0093 (Figure 4).

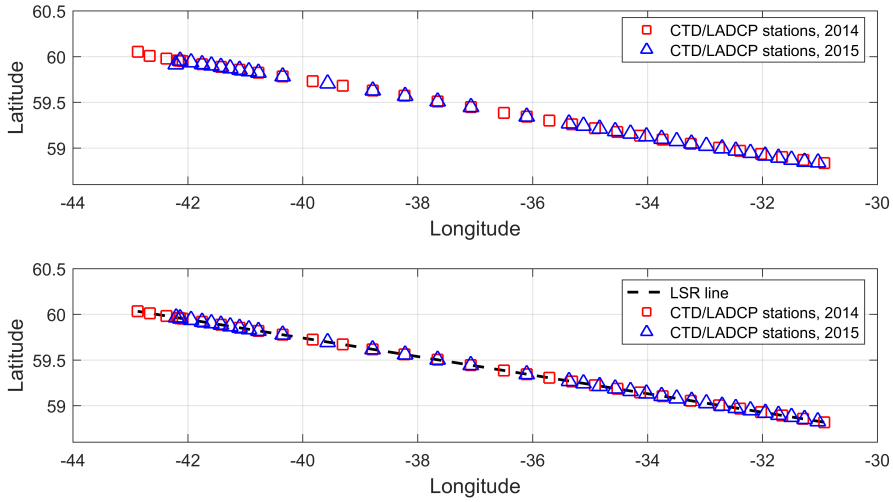

FIGURE 4: a) Initial position of CTD/LADCP stations for 2014 and 2015, and b) Projected position of CTD/LADCP stations for 2014 and 2015 on the LSR line. Stations close to the coast of Greenland were not repeated in 2015 due to the extent of sea ice further from the coast.

In each station a calibrated SBE (Sea Bird Electronics) 911plus CTD (Conductivity, Temperature and Depth) profiler providing 24 Hz sampling, was used to measure pressure (dbar), temperature (°C), salinity (psu), and turbidity (ftu) profiles. The CTD was mounted in a rack, with 20 Niskin water bottles to take samples for salinity and oxygen calibration, and nutrient samples. Attached to the CTD, an LADCP (Lowered Acoustic Doppler Current Profiler) provided direct velocity measurements. Individual CTD casts were processed with SBE Seasoft software and calibrated against in-situ salinity samples. The data where then averaged on either 1dbar (2015) or 2dbar (2014) bins for regular use and to 1 Hz averages for LADCP processing. Finally, a second (local) bathymetric profile was acquired with the assumption that during the cruise the last measurement on each CTD/LADCP station was taken 7m above the bottom of the ocean. This profile was then used to correct the profile from Etopo, wherever Etopo derived bathymetry exceeded local bathymetry. This final version was adopted for plotting purposes of the hydrographic data.

2.1.1. Hydrographic observations from the Irminger Basin

Initial CTD data were used to calculate absolute salinity (g kg^{-1}), conservative temperature (°C), and potential density anomaly (kg m^{-3}) relative to the surface through TEOS-10 (http://www.teos-10.org) thermodynamic equation which "is based on a Gibbs function formulation from which all thermodynamic properties of seawater (density, enthalpy, entropy sound speed, etc.) can be derived in a thermodynamically consistent manner" (McDougall and Barker, 2011). This equation was adopted by the Intergovernmental Oceanographic Commission at its 25^{th} Assembly in June 2009. More specifically, conservative temperature is not a true temperature but an energy (enthalpy) scaled to have units of temperature and it is conserved during adiabatic processes. Absolute Salinity is defined as the mass fraction of sea salt in seawater and is a more accurate representation of salinity. Following de Jong et al.,(2012), planetary potential vorticity (PPV) was calculated as follows: First, in order to remove the effect of small scale noise and short term fluctuations, pressure, absolute salinity and conservative temperature fields were smoothed with a running mean of 50dB and subsampled every 25dB. From these data, the Brunt–Väisälä frequency (N^2) was calculated with the equation $N^2 = \frac{g^2\rho(\beta^{\Theta}\Delta S_A - \alpha^{\Theta}\Delta\Theta)}{\Delta P}$, where: ΔS_A and $\Delta\Theta$ are the difference in Absolute Salinity and Conservative temperature of particles in the water column, separated in the vertical by pressure ΔP, g is the gravitational acceleration, ρ the density, β_θ and α_θ are the saline contraction and thermal expansion coefficients. This frequency field was subsequently used to construct the PPV ($PPV = f * \frac{N^2}{g}$) field, under the assumption that horizontal gradients are weaker than vertical ones and thus relative vorticity(ζ) is negligible ($\zeta = \frac{dv}{dx} - \frac{du}{dy}$). Conservative temperature (C°), absolute salinity (g kg^{-1}), potential density relative to the surface (kg m^{-3}) and planetary potential vorticity (10^{-12} $m^{-1}s^{-1}$) were interpolated with a linear interpolant to a standard grid for 2015 (1.88km X 1m) and for 2014 (1.88Km X 2m) respectively.

2.1.2. Direct velocity observations from the Irminger basin

Initially, both components of the direct velocity from the LADCP, with the effect of tidal currents already removed, were rotated with an angle $\phi = -10°$in order to obtain the across and along LSR components respectively. Then, the dynamic height anomaly was computed (GSW toolbox – MATLAB), as the integral of specific volume anomaly from the pressure p of the "bottle" to the reference pressure of the surface (0 dbar). Using this streamfunction (dynamic height anomaly) geostrophic velocities relative to the surface were obtained at the mid-point between the locations of each station pair along the section. Velocities relative to the bottom were calculated with the assumption that the flow there is zero (level of no motion) by subtracting the last (bottom) value of each station from the whole profile of that station.

Geostrophic velocities calculated from hydrographic data are insufficient to define the complete velocity field. The necessary assumption of a reference level where velocities are zero is of course fragile and thereby the next step is to reference geostrophic velocities to barotropic velocities. This was achieved with the help of directly measured velocities (LADCP) as follows: From each pair of subsequent LADCP stations a mean LADCP-profile was calculated. Then the mean value of this mean-profile along with the mean value of the corresponding geostrophic velocity profile were computed, taking in account values

of the two fields from the (approximate) common top pressure level to the (approximate) common bottom pressure level. Subtraction of the latter from the first,

$$V_{barotropic} = V_{LADCP} - V_{geostrophic},$$

led to the barotropic correction term which was then added to the original vertical profile of the geostrophic velocity (relative to the bottom). This way we constructed the absolute geostrophic velocity profile for that mid-point between two CTD/LADCP stations. Following the same procedure for all the station pairs, the absolute geostrophic velocity field for the whole section was obtained (Figure 5). We have to note here that in 2014, the CTD station with coordinates longitude=-42.66, latitude=60.00 did not include LADCP measurements and thus was excluded from the above calculations.

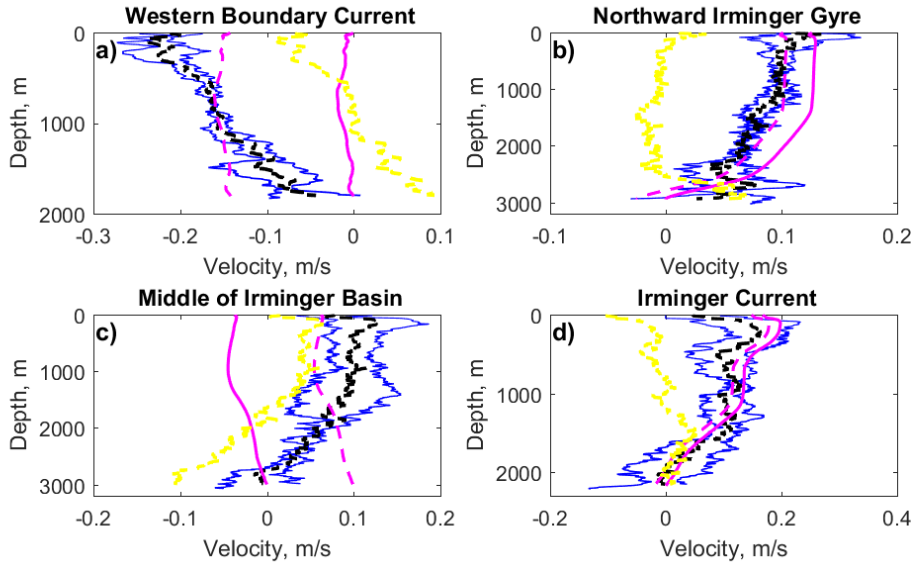

FIGURE 5: Demonstration of the barotropic adjustment to the geostrophic velocities. Solid blue lines indicate subsequent vertical profiles of the direct velocity (LADCP) field, whereas the dashed black line is the mean of those. The solid purple line shows the initial vertical profile of the geostrophic velocity relative to the bottom for the mid-point of the CTD/LADCP station pair. Next, the dashed purple line is the vertical profile of the absolute geostrophic velocity that resulted after the barotropic adjustment. Finally, the solid yellow line indicates the vertical profile of the ageostrophic component.

Finally, the absolute geostrophic velocity field was interpolated with a linear interpolant to a standard grid for 2015 (1.88km X 1m) and 2014 (1.88km X 2m) respectively. Errors resulting from this process were in the order of $\sim 10^{-3}$ m s^{-1}.

2.2. Results: Atmospheric forcing during the winter of 2014-2015

The winter of 2014-2015 is of particular interest for the Irminger Sea. During this period, the local atmospheric forcing was significantly higher than the previous winters. To illustrate the above the following datasets were used:

- Monthly mean NAO index, provided by the National Oceanic and Atmospheric Administration (NOAA, USA) through the website:
  $http://www.cpc.ncep.noaa.gov/products/precip/CWlink/pna/nao_index_ensm.shtml$.

- Monthly mean wind stress curl (10^{-7} Pa m^{-1}) at $\sim$ 60°N across the Irminger basin. At first the monthly mean zonal (T_χ) and meridional (T_y) components of the wind stress were calculated as follows:

$$T_\chi = \rho_o \cdot cd \cdot U \cdot U_{10} \text{ and } T_y = \rho_o \cdot cd \cdot U \cdot V_{10}$$

  where ρ_o=1.22 kg m^{-3} is the air density, cd is the non-dimensional drag coefficient, U is the wind speed magnitude ($U = \sqrt{u_{10}^2 + v_{10}^2}$) and u_{10} and v_{10} the zonal and meridional components of the wind speed 10m above the surface of the ocean. The drag coefficient equals to 10^{-3} if $|U| < 7.5$ and $(0.61 + 0.063 \cdot |U| \cdot 10^{-3})$ if $|U| >= 7.5$. Then the monthly mean wind stress curl (ξ) was found with the equation $\xi = \frac{dT_y}{dx}$ - $\frac{dT_\chi}{dy}$, solved by finite difference. The two components of the wind speed 10m above the sea (u_{10}, v_{10}) were monthly means of daily forecast accumulations of ERA interim data, extracted from the European Center for Medium-Range Weather Forecasts (ECMWF) online dataset.

- Monthly mean downward total net heat flux (Qnet, W m^{-2}). It was computed as Qnet=SR-LR-LHF-SHF, where SR, LR, LHF and SHF denote net downward shortwave radiation, net upward longwave radiation, latent heat flux and sensible heat flux respectively. The above fields were provided from the North American Regional Reanalysis (NARR) project of NOAA
  ($http://www.esrl.noaa.gov/psd/data/gridded/data.narr.monolevel.html$).

The NAO index exhibited high positive values for four consecutive months (December 2014 – March 2015), something certainly not common (Figure 6, panel a). The previous winters were characterized by low (positive) or even some times negative NAO index. This enhanced local forcing induced high positive wind stress curl (values greater than 10^{-7} Pa m^{-1}) over the Irminger Sea for at least three consecutive months (Figure 6, panel b). At the same period the heat loss from the ocean to the atmosphere was anomalously large (Figure 6, panel c), with a winter (December 2014 – March 2015) mean of -287.65 W m^{-2}, and a maximum of -400 W m^{-2} during January 2015.

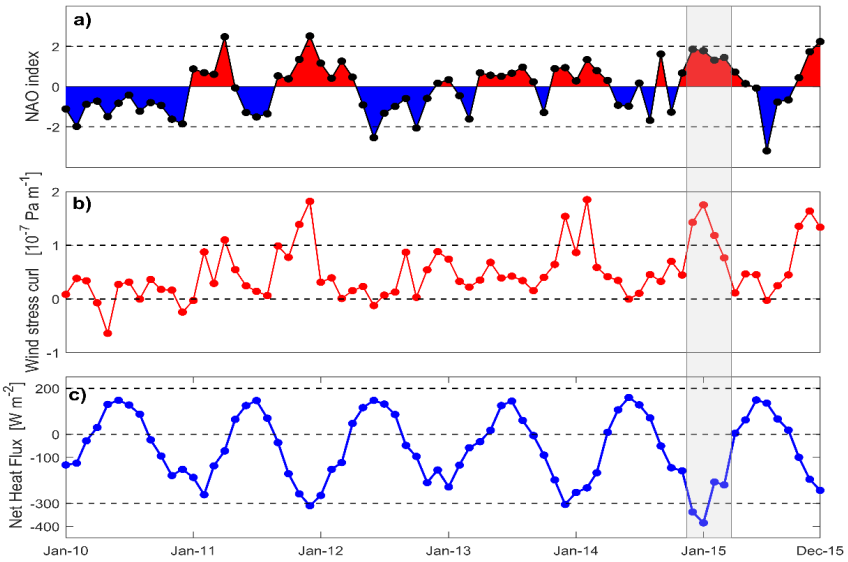

FIGURE 6: Illustration of the evolution in time, from January 2010 to December 2015, of three different variables: a) North Atlantic Oscillation (NAO) index. Positive/negative values of the index are illustrated with red/blue color. b) Wind stress curl (10^{-7} Pa m^{-1}) at $\sim$ 60°N across the Irminger Sea. c) Net Heat Flux (W m^{-2}) at $\sim$ 60°N across the Irminger Sea. Positive/negative values denote net heat flux towards the ocean/atmosphere in the section. The shaded grey area shows the winter of 2014-2015 (December 2014-March 2015), that is of interest here.

All the above are favorable conditions for convection to happen in the Irminger Sea. The preceding winters (2010-2014), heat flux towards the atmosphere was much lower with a winter mean value of -195.3 W m^{-2} and maximum values that did not exceed -300 W m^{-2}. Finally, this shift in atmospheric forcing is reversely comparable to the one that took place in the basin from the early 1990s (1990-1994, high NAO index) to the early 2000s (2000-2004, low NAO index) and is described in Våge et al., 2011.

2.3. Results: Evidence of convective activity

Strong atmospheric forcing during winter 2014-2015 induced increased heat loss from the ocean to the atmosphere than the previous winters (Figure 6). As a result, LSW could have been formed via deep convection in the Irminger Gyre. LSW is usually formed during deep convection events in the Labrador basin and is transported to the Irminger basin in timescales of 1 to 2 years (Yashayaev et.al., 2007). Its characteristics depend on the strength and the duration of the convection events and planetary potential vorticity, a measure of the stratification of the water column, can be used as its tracer. In July 2014, conservative temperature in the basin was significantly higher than in July 2015. Especially in the eastern part of the basin, close to the Reykjanes Ridge where the Irminger Current lies, temperature dropped as much as 2°C. In July 2015, a local temperature minimum was observed on the central and eastern part of the basin, concentrated between 1000-1500m depth. The 27.7 density line (upper part of the water column) in July 2015, in this part of the basin, was raised close to the surface and the 27.8 density line, that separates the

middle with the deep part of the water column, was lowered in comparison with the situation in July 2014. This is a clear sign that a weakly stratified part of the ocean was created in-between these density lines. This is illustrated clearly as a big area of almost uniform density between the 27.74 and 27.75 density contours (magenta dashed lines) in Figure 7, bottom panel.

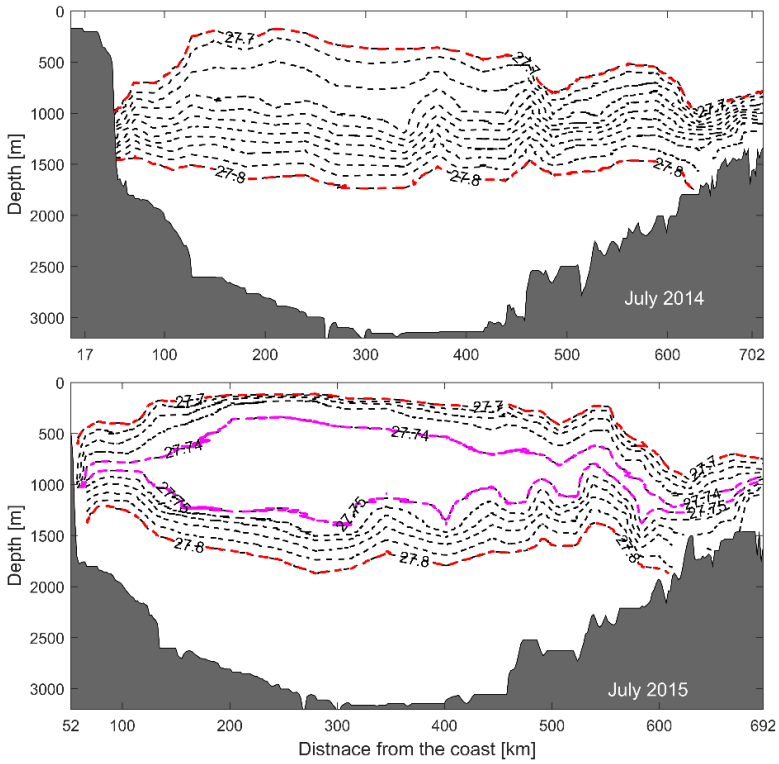

FIGURE 7: Illustration of changes in potential density relative to the surface from July 2014 to July 2015. Potential density relative to the surface (σ_0) contours from 27.7 $kg\ m^{-3}$ to 27.8 $kg\ m^{-3}$ are drawn with a step of 0.01 $kg\ m^{-3}$. Red dashed lines indicate the 27.7 $kg\ m^{-3}$ (upper limit) and the 27.8 $kg\ m^{-3}$ (lower limit) density contours. Magenta dashed lines enclose an area of potential density between 27.74 and 27.75 $kg\ m^{-3}$.

The above can also be concluded from the inspection of the planetary potential vorticity (PPV) field (Figure 8, bottom panels). In July 2015, a large area with PPV values less than 4*10^{-12} $m^{-1}s^{-1}$ and minimum values very close to zero (0) was evident in depths from 300 to 1500m depth. Such low PPV values infer extremely low stratification and indicate that local convective activity has occured (Pickart et.al., 2002 & 2003). The previous summer PPV values in the same area were significantly higher, with minimum values concentrated in two tiny areas, around 4*10^{-12} $m^{-1}s^{-1}$. Thus, the denser, colder and more oxygenated LSW in the center and eastern side of the basin confined from the 4*10^{-12} $m^{-1}s^{-1}$ isoline of density, found in the summer of 2015, is argued to be convectively formed in the area. Its characteristics are: Conservative temperature: 2.88 °C - 3.28 °C, Absolute salinity: 35.01 $\frac{g}{kg}$ - 35.05 $\frac{g}{kg}$, dissolved Oxygen: 290 $\frac{umol}{kg}$ - 300 $\frac{umol}{kg}$. The lighter, warmer and less oxygenated water found in the same area in the summer of 2014 is likely LSW formed in the Labrador and advected to the Irminger Sea.

The above are in agreement with the findings of de Jong and de Steur (2016). Using data from a mooring located in the center of the Irminger Gyre, they showed that very deep convection took place in the central Irminger gyre evidenced by data from a profiling mooring there.

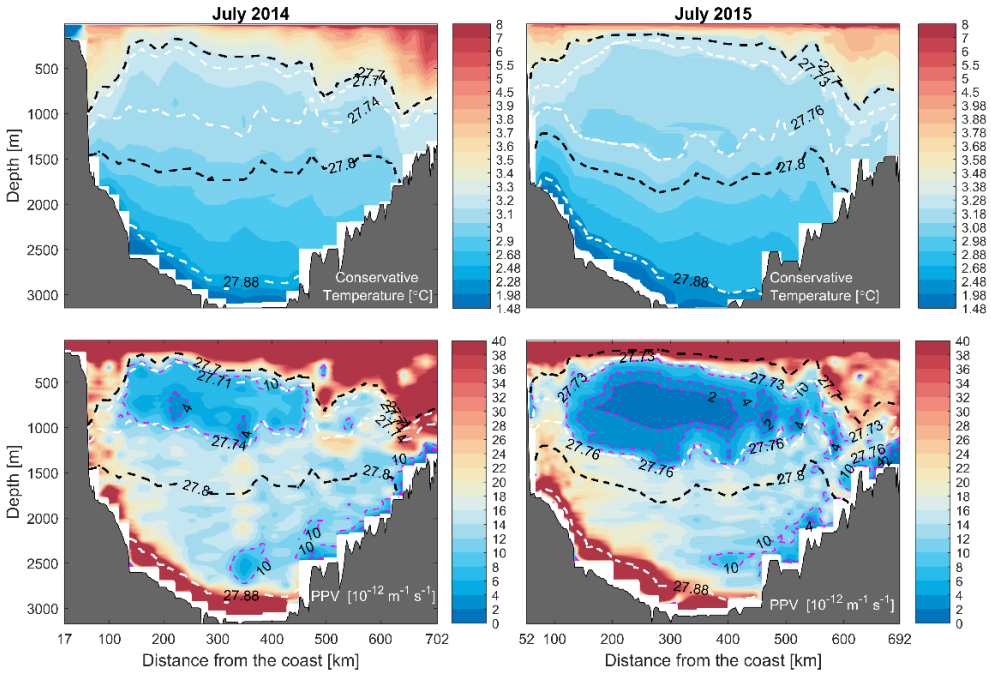

FIGURE 8: Changes in Conservative Temperature (upper plots) and Planetary Potential Vorticity (lower plots) between July 2014 and July 2015. Black dashed lines distinguish the water column in upper (σ_0<27.7 kg m^{-3}), middle (27.7 kg m^{-3} < σ_0<27.8 kg m^{-3}) and deep (σ_0>27.8 kg m^{-3}) ocean in terms of potential density relative to the surface (σ_0). White dashed-lines enclose a class of intermediate water (LSW) in the upper 1500m and a class of deep water (DSOW) below 2000m. Magenta dashed lines denote lines of equal PPV (10^{-12} $m^{-1}s^{-1}$).

Of interest is also the change in the PPV field in the eastern side of the basin. One can notice that in the location where we expect to find the Irminger Current stratification is much weaker in July 2015 than in July 2014. The lateral spread of the mentioned intermediate water mass (LSW) in conjunction with intense surface heat loss was likely the cause of this decrease.

2.4. Results: Changes in the circulation

Increased convective activity has been linked with the expansion (Hatun et al., 2005; Bersch et al., 2007) and spin-up (Hakkinen et al., 2004) of the Subpolar Gyre. Model studies have also supported the link between convection in the Subpolar Gyre and changes in the strength of the Atlantic Meridional Overturning Circulation (AMOC). Most of these studies are concerned with inter-annual to multi-decadal time scales. There is no clear indication on how and by how much the local convective activity affects the circulation in the Irminger basin or to a broader extend circulation in the Subpolar Gyre, in short time scales.

2.4.1. Absolute geostrophic velocities

The main circulation features in the Irminger Sea (Figure 9), are:

(a) The Irminger Current: Recognized as a surface-intensified and predominantly baroclinic northward flow on the west of the Reykjanes Ridge (eastern Irminger basin). It supplies the basin with warm and saline waters of Atlantic origin.

(b) The Irminger Gyre: A barotropic feature, defined as the narrow cyclonic recirculation on the western side of the southern Irminger basin.

(c) Western Boundary Current: The southward flow on the western boundary of the Irminger basin close to the east coast of Greenland.

Although the Irminger Gyre and the Western Boundary Current are important features of the circulation in the Irminger basin, only changes of the Irminger Current are of interest here. The Irminger Current is found in an area enclosed in the zero isotach (red solid line) around 620km and around 560km off the coast of Greenland for July 2014 and July 2015 respectively. The core of the Irminger Current occupies the shallow layer (σ_0<27.7 kg m^{-3}) of the ocean close to the Reykjanes Ridge. In the time period between the two hydrographic transects, the core of the current moved from around 620km to around 560km off the coast of Greenland and became stronger, consistent with the notion of a strengthen Subpolar Gyre.Despite this, its total strength did not change significantly, because at the same time its spatial extend decreased from 130km in 2014, to 80km in 2015. A peculiar feature in the basin that exists in 2014, but not in 2015, is another surface intensified flow around 490km off the coast off Greenland and 60km to the west of the Irminger Current. These "snapshots" off the ocean do not provide sufficient information as to whether this feature is another branch of the Irminger Current or just a temporal oceanic feature. Våge et al.,(2011) contrasted mean absolute geostrophic fields from the early 1990s (high NAO index) to the early 2000s (low NAO index). For the 1990s, he found that the Irminger Current had one core and was located $\sim$ 600km off the coast of Greenland. This outcome is in good agreement with the situation described here for July 2015 and the difference in the location of the current can be attributed to the fact that Våge's absolutely geostrophic field is a mean of 5 years. On the other hand, during the 2000s he found that the Irminger Current, even though on the same location, had two deep extensions. This was not the case in July 2014, when the IC was found here some km east of its location in July 2015.

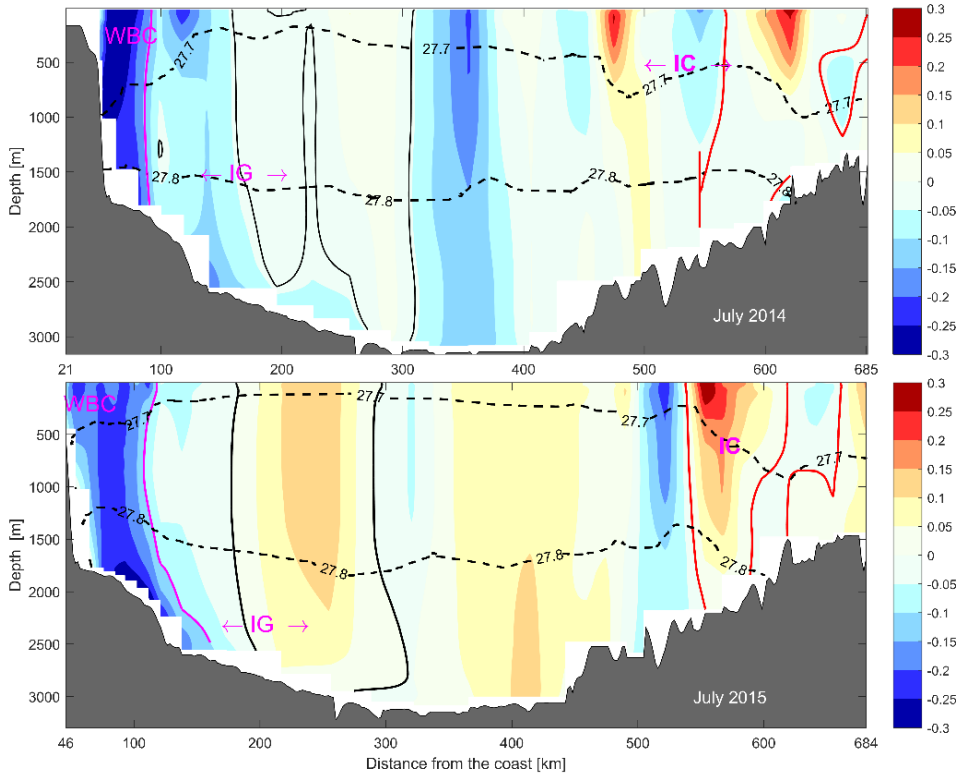

FIGURE 9: Absolute geostrophic velocity field ($\frac{m}{s}$) for July 2014 (upper plot) and July 2015 (lower plot). Positive values indicate northward and negative values southward flow respectively. Zero (0) isotachs are presented as solid black (IG) and red lines (IC) whereas the solid magenta line represents the -0.1 isotach on the western side of the basin. Black dashed lines, represent contours of potential density relative to the surface (σ_0). The upper density line (27.7 kg m^{-3}) separates the surface part of the water column from the intermediate one, and the lower density line (27.8 kg m^{-3}) separates the intermediate part of the water column from the deep one.

This difference could arise from the fact that Våge et al. derived the absolute geostrophic field with different methods than the ones applied here. He referenced the geostrophic velocities, using AVISO gridded surface velocities. His final results were based on the sea surface height method (SSH) which results in a much smoother field.

2.4.2. Geostrophic Volume Transport

Geostrophic transport for each box in the standard grid of each section, was calculated by multiplying the absolute geostrophic velocity on the box with the size (horizontal distance in meters, vertical extent in meters) of the box. Geostrophic transport was calculated for the main circulation features in the Irminger basin (Table 1).

- The Irminger Current: Its transport is calculated from the area enclosed in the zero isotach (red solid line) on the eastern side of the Irminger basin.
- The Irminger Gyre: Its transport is calculated from the northward flow between 200-300km off the coast of Greenland (black solid line).

- Western Boundary Current: Its transport is calculated from the southward flow, on the south-western Irminger Sea, west of the -0.1 isotach (magenta solid line).

TABLE 1: Positive values indicate northward and negative values southward volume transport respectively. Values in parenthesis represent upper 500m transport for the Irminger and upper 1500m transport for the Western Boundary Current.

	2014	2015
Irminger Current	8.12 (4.71) Sverdrup	7.46 (4.09) Sverdrup
Irminger Gyre	9.86 Sverdrup	15.43 Sverdrup
Western Boundary Current	-8.98 (-8.80) Sverdrup	-14.54 (-10.21) Sverdrup

In 2014 the extra stations close to the coast of Greenland, that did not exist in 2015, contributed -0.34 Sv to the close-to-shelf transport of the WBC. To enable better comparison between the two years this shelf transport was subtracted from the total WBC transport for 2014. In Chapter 4, these estimates are going to be compared with the estimates of Våge et al., (2011) and the transport calculated from the year-round velocity field.

Chapter 3 - Variability of the Irminger Current

In order to characterize the variability of any oceanic phenomena, first a reference state needs to be established. Secondly, the observational record of these phenomena should (preferably) be much longer than the time scale of the variability of interest. The results of this thesis can only be compared to previous estimates from summer hydrographic sections because this is the first ever (full depth) time series trying to quantify the spatial and temporal variability of the Irminger Current. Initially a "first look" on the directional preference as well as the spectra of the velocities will provide us a first view of the variability on the section, and serves as a guide on how to proceed with further analysis of the velocity field. Monthly variability, seasonal changes as well as changes in temperature and the velocity field follow.

3.1. Data and methods

3.1.1. Mooring data from the Irminger Current

Mooring data used for Chapter 3 and 4 come from a mooring line located on the eastern side of the Irminger basin, west of the Reykjanes Ridge, that covers the Irminger Current and consists of four moorings namely IC_1,IC_2, IC_3 and IC_4. Instrumentation on this line includes upward-looking ADCPs (Acoustic Doppler Current Profilers), CMs (Current Meters) and MCTDs (Moored CTDs) in various depths (Figure 10). ADCPs provide high-resolution time series of velocity measurements in the upper 450-500 meters of the ocean, whereas CMs provide time series of point-velocity measurements at specific depths deeper in the water column. MCTD's provide time series of temperature (°C) and salinity (psu) from which other variables of interest were derived. The instruments were deployed between July^{8th} and July^{11th}, 2014 by research vessel Knorr Cruise and were recovered and redeployed between July^{8th} and July^{11th}, 2015 by research vessel Pelagia. This recovery, resulted in the first year-round full-depth time series of the line from this section.

3.1.1.1. Treatment of velocity (ADCP, CM) measurements

Due to various technical issues of the instruments the current meters at 725m and 1725m depth in IC_2 stopped working at the end of September, 2014 and thus their very short time series were discarded. The current meter at 725m in IC_3 stopped working around mid-May,2015 but high correlation of its time series up till then with the time series of the current meter at 975m in IC_3 led to its expansion in time through first order polynomial fitting. Additionally, time series had different starting and/or ending date as well as missing values. Thereby they were reduced to fit the shortest one lasting from July^{12th}, 2014 to July^{3rd} 2015 and measurement gaps were filled using linear interpolation in time. Outliers in each individual time series were detected with the implementation of Grubbs outlier test, which evaluates if any one observation belongs to the sample population or not. If the G (G=$\frac{(x_o-\bar{x})}{std}$ if x_o>$\bar{x}$ and $G = \frac{(\bar{x}-x_o)}{std}$ if $x_o < \bar{x}$) value of an observation x_o exceeds a critical value determined by the observation number and the significance level for determination of outliers, the observation was considered an outlier and removed accordingly.

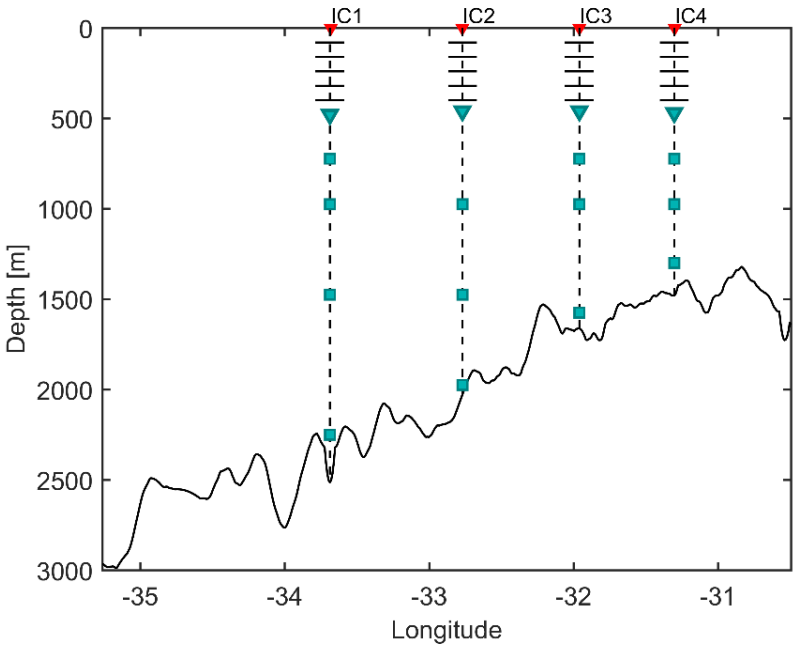

FIGURE 10: Sketch of the four moorings on the west side of the Reykjanes Ridge (eastern Irminger Basin). Triangles represent upward looking ADCPs which map approximately the upper 450m of the water column, in bins illustrated here with small straight lines above the ADCPs. Squares in various depths below the ADCPs represent Current Meters (CMs). MCTDs' were mounted on all the above instruments and at 70m depth in every mooring.

Because the rate of sampling was faster for the CMs (1200 sec.) than the ADCPs (3600 sec), measurements obtained from the CMs were subsampled to match the sampling interval of the ADCPs. High frequency components of the velocity field are not of interest here. Consequently, inertial oscillations and tidal motions were filtered out using a 4th order low-pass Butterworth filter with cut-off period of 40 hours resulting in a cut-off frequency fc=6.94*10^{-6} Hz (Figure 11). A Butterworth filter is a low-pas filter with an amplitude response of

$$|H(\omega)| = \frac{1}{\sqrt{1+(\frac{\omega}{\omega c})^{2n}}},$$

where ω_c is the cut-off frequency of the filter and n is the order of the filter. Matlab's butter algorithm, that was used to construct the filter, expects a normalized frequency between zero (0) and one (1) where one is the Nyquist frequency (f_N). Hence, the input normalized frequency for the butter function was $\frac{f_c}{f_N}$. Moreover, the order of the filter (n) determines the rate of transition from high to low filter gain in a way that higher order leads to faster transition.

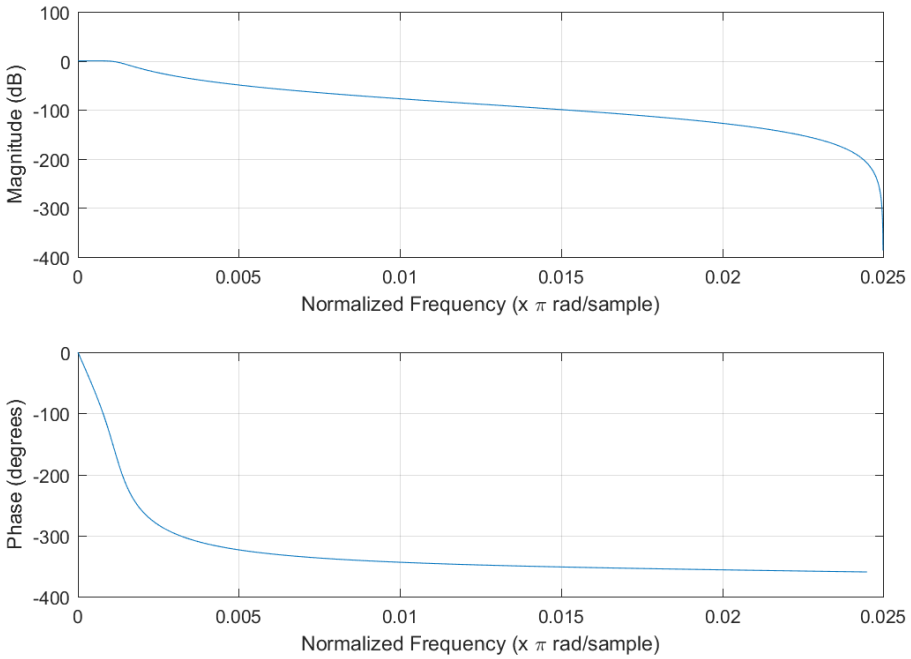

FIGURE 11: Magnitude (upper plot) and phase response (lower plot) of the low-pass Butterworth filter versus the normalized frequency multiplied by π rad sample-1.

Next, daily mean values were computed for the existing time series of the two components of the velocity field. Basic statistics of these daily mean time series are presented on Tables 2 and 3.

TABLE 2: Mean year-round south (negative) - north (positive) velocities (cm s^{-1}) and their standard deviation (in parenthesis) for the four moorings, from daily time series at specific depths on each individual mooring. ADCP and CM measurements are noted in the upper and lower part of the table respectively.

	IC_1	IC_2	IC_3	IC_4
100 m	1.81(13.92)	0.69(15.04)	5.64(14.05)	8.57(12.91)
400 m	2.54(10.84)	0.82(10.77)	4.19(9.96)	7.60(10.33)
725 m	2.03(7.55)	-	1.21(5.20)	4.07(5.25)
975 m	2.16(7.01)	0.08(5.51)	1.00(4.12)	4.42(4.31)
1300 m	-	-	-	5.40(4.61)
1475 m	2.23(4.38)	0.93(3.50)	-	-
1575 m	-	-	1.10(3.58)	-
1975 m	-	3.70(4.28)	-	-
2250 m	2.65(4.19)	-	-	-
2480 m	2.62(6.55)	-	-	-

TABLE 3: Mean year-round west (negative) - east (positive) velocities (cm s^{-1}) and their standard deviation (in parenthesis) for the four moorings, from daily time series at specific depths on each individual mooring. ADCP and CM measurements are noted in the upper and lower part of the table respectively.

	IC_1	IC_2	IC_3	IC_4
100 m	3.36(15.85)	2.66(13.06)	2.19(12.60)	2.13(11.32)
400 m	2.54(10.84)	0.82(10.77)	4.19(9.96)	7.60(10.33)
725 m	1.16(8.30)	-	0.24(4.92)	0.44(4.68)
975 m	1.24 (7.75)	-0.02(5.02)	-0.29(4.48)	0.43(3.26)
1300 m	-	-	-	2.27(2.76)
1475 m	0.70(4.73)	0.51(2.94)	-	-
1575 m	-	-	-1.09(2.48)	-
1975 m	-	-0.23(2.29)	-	-
2250 m	-0.52(2.05)	-	-	-
2480 m	-0.65(1.70)	-	-	-

3.1.1.2. Treatment of MCTD measurements

MCTD derived time series for Conservative Temperature (°C), Absolute Salinity (g kg^{-1}) and potential density relative to the surface (kg m^{-3}) were reduced to fit the length of the velocity time series ($July^{12th}$, 2014 to $July^{3rd}$ 2015). Gaps in individual time series were filled with linear interpolation in time. The MCTD at 70m in IC_1 dropped from its initial position down to 175m depth and remained there until it was collected in July 2015. Additionally, MCTD's at 70m in IC_2, IC_3 and IC_4 begun the recording of measurements on early October, 2014 and mid to late July 2014 respectively. These time series were extended back in time, using first order polynomial fitting, exploiting the fact that they were highly correlated with full time series at 475m depth in the moorings of interest. At last, daily mean values were computed for each variable.

3.1.1.3. Gridding

In order to compute the velocity field for the whole section, and later the volume transport, various techniques were employed. At first, interpolation was carried out in the vertical between subsequent instruments on each individual mooring. Then, velocities were extrapolated down to the bottom and up to the surface of the ocean. The final step, was to spatially interpolate in the horizontal between the locations of the moorings. All the above procedures should be performed in an appropriate grid that includes the bottom topography of the section. Initially, the across-section field was placed in a 3D matrix (depth x distance x time) with constant binning both in the vertical (10m) and in the horizontal (2.1km). For each time step, measurements were placed on this matrix in such a way as to account for fluctuations in the position (in depth) of the instruments. Pressure data that were extracted from the current meters were unreliable and as such were discarded. Depth fluctuations of the ADCPs' due to oceanic motions were used to calculate the displacement of the current meters (Figure 12). That was possible under the assumption that the line that was connecting the instrumentation on each individual mooring was straight at all time steps when displaced. The ADCPs' disposition was more apparent during the winter period and especially during February 2015.

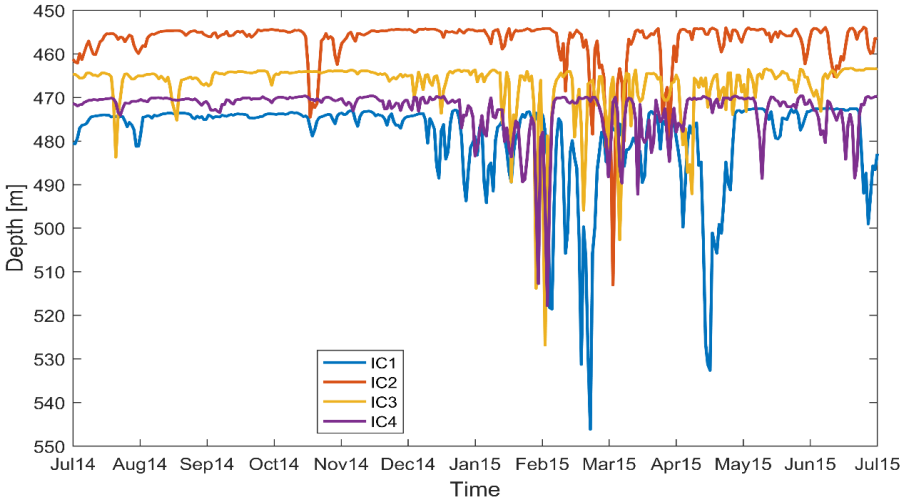

FIGURE 12: ADCPs' depth fluctuations for the four moorings from July 2014 to July 2015.

Then, cross-correlations among the instruments were determined with the computation of a correlation coefficient, both in the vertical and in the horizontal, to support spatial interpolations and the results are presented below (Figure 13). On the one hand, correlation in the vertical is very high in the upper 1500m and high to poor in depths below that level on each individual mooring. On the other hand, in the horizontal correlations are low except between the upper 1500m of IC_1 and IC_2 where poor anti-correlations are observed. A p-value is the measure of the probability of getting a correlation as large as the observed value by random chance, when the true correlation is zero. If p is less than 0.05, then the correlation is considered significant. All the correlations that are of interest were significant under the p-value probability test.

	IC1-400m	IC1-725m	IC1-975m	IC1-1475m	IC1-2250m	IC1-2480m	IC2-100m	IC2-400m	IC2-975m	IC2-1475m	IC2-1975m	IC3-100m	IC3-400m	IC3-725m	IC3-975m	IC3-1575m	IC4-100m	IC4-400m	IC4-725m	IC4-975m	IC4-1300m
IC1-100m	0.93	0.7	0.63	0.57	0.08	0.01	-0.33	-0.39	-0.26	-0.19	0.12	0.09	0.08	0.25	0.26	0.15	-0.02	-0.07	-0.02	-0.05	-0.1
IC1-400m	1	0.81	0.75	0.67	0.12	0	-0.44	-0.48	-0.39	-0.34	0.09	0.06	0.08	0.27	0.28	0.17	-0.08	-0.12	-0.12	-0.16	-0.2
IC1-725m	-	1	0.98	0.91	0.36	0.22	-0.51	-0.52	-0.48	-0.45	-0.02	-0.01	0.04	0.19	0.21	0.15	-0.14	-0.14	-0.18	-0.24	-0.22
IC1-975m	-	-	1	0.93	0.41	0.27	-0.51	-0.51	-0.49	-0.46	-0.03	-0.05	0	0.16	0.19	0.17	-0.14	-0.12	-0.18	-0.24	-0.21
IC1-1475m	-	-	-	1	0.55	0.39	-0.55	-0.53	-0.5	-0.45	-0.03	-0.03	0.02	0.15	0.2	0.11	-0.1	-0.09	-0.16	-0.22	-0.19
IC1-2250m	-	-	-	-	1	0.85	-0.39	-0.35	-0.36	-0.29	-0.04	0.12	0.16	0.09	0.11	0.06	-0.01	-0.01	-0.11	-0.13	0
IC1-2480m	-	-	-	-	-	1	-0.22	-0.18	-0.15	-0.1	0.01	0.07	0.09	0.03	0.06	0.04	0.02	0.02	-0.07	-0.07	0.07
IC2-100m	-	-	-	-	-	-	1	0.94	0.74	0.6	-0.03	-0.06	-0.11	-0.09	-0.1	-0.04	0.11	0.1	0.15	0.24	0.23
IC2-400m	-	-	-	-	-	-	-	1	0.79	0.59	-0.09	-0.1	-0.16	-0.17	-0.18	-0.12	0.12	0.12	0.16	0.23	0.24
IC2-975m	-	-	-	-	-	-	-	-	1	0.87	0.12	0	-0.11	-0.11	-0.08	-0.08	0.15	0.11	0.19	0.29	0.3
IC2-1475m	-	-	-	-	-	-	-	-	-	1	0.34	0.02	-0.07	-0.07	-0.04	-0.01	0.16	0.11	0.22	0.32	0.28
IC2-1975m	-	-	-	-	-	-	-	-	-	-	1	0.01	0.05	0.05	0.03	0.07	0.08	0.07	0.11	0.12	0.04
IC3-100m	-	-	-	-	-	-	-	-	-	-	-	1	0.9	0.61	0.49	0.2	0.06	0.02	0.08	0.16	0.2
IC3-400m	-	-	-	-	-	-	-	-	-	-	-	-	1	0.76	0.63	0.25	-0.03	-0.06	-0.03	0.06	0.1
IC3-725m	-	-	-	-	-	-	-	-	-	-	-	-	-	1	0.93	0.51	-0.11	-0.15	-0.16	-0.06	0
IC3-975m	-	-	-	-	-	-	-	-	-	-	-	-	-	-	1	0.58	-0.08	-0.14	-0.15	-0.06	0.02
IC3-1575m	-	-	-	-	-	-	-	-	-	-	-	-	-	-	-	1	0	-0.02	0.01	0.06	0.08
IC4-100m	-	-	-	-	-	-	-	-	-	-	-	-	-	-	-	-	1	0.92	0.75	0.49	0.3
IC4-400m	-	-	-	-	-	-	-	-	-	-	-	-	-	-	-	-	-	1	0.86	0.57	0.35
IC4-725m	-	-	-	-	-	-	-	-	-	-	-	-	-	-	-	-	-	-	1	0.8	0.52
IC4-975m	-	-	-	-	-	-	-	-	-	-	-	-	-	-	-	-	-	-	-	1	0.8

FIGURE 13: Correlation coefficients (C.C.) indicate the amount of correlation between time series among all instruments in the section. Highlighted with red and orange color is high (C.C.>0.65) and poor (0.50<C.C.<0.65) correlations respectively. Additionally, highlighted with green color are values that indicate poor anti-correlations (C.C.~ 0.50).

The above information was used as a guide to linearly interpolate the velocity in the vertical between subsequent instruments on each individual mooring. The results of this process are presented on Figure 14.

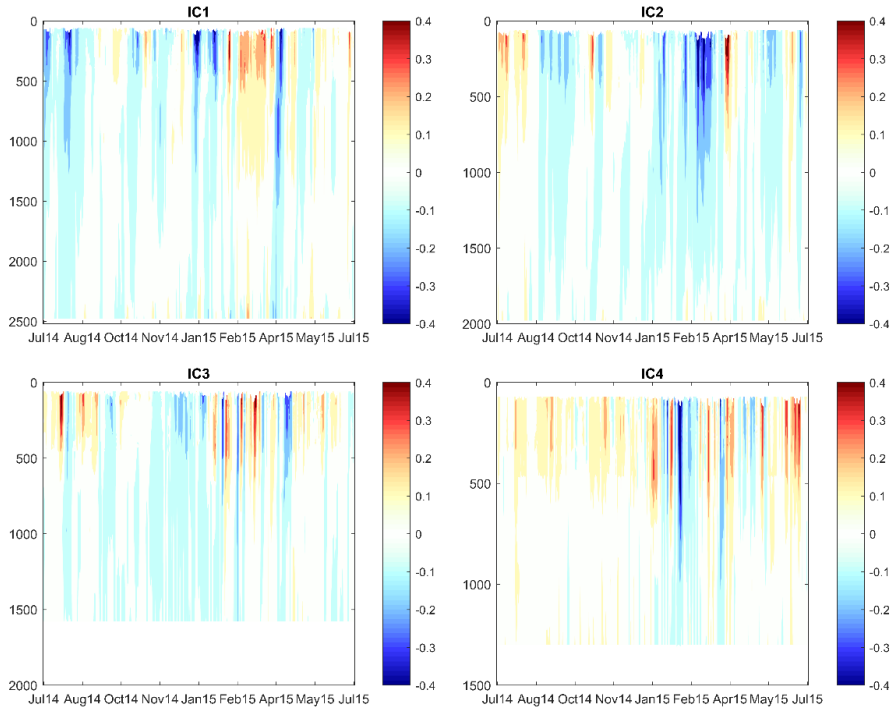

FIGURE 14: Vertically (in depth) interpolated velocities (m s^{-1}) for the four moorings. Positive values indicate northward and negative values southward flow.

The next step, was to move the full vertical profiles in time, in an appropriate grid. That was necessary in order: a) to fill the gaps between the deepest instrument on every mooring and the bottom topography and b) to interpolate in the horizontal between the moorings. This way the full-depth velocity field in the section could be constructed and later used to compute the volume transport. Three grids (Table 4) were tested for their consistency in retaining the gradients of the velocity field in two crucial transition depths: the one between each ADCP (high resolution measurements) and the first CM (point measurements) and the last depth with measurements for all the moorings (1300m). Approximately, this is also the location where a shift was earlier documented from high to poor vertical correlations.

TABLE 4: Characteristics of the vertical gridding of three grids that were tested. Numbers in parenthesis represent the number of the bins. In the horizontal all the grids had the same constant binning every 2.1km

	Constant binning	Bathymetry following contours
First Grid	0-200m (21)	Below 200m (10)
Second Grid	0-500m (51)	Below 500m (10)
Third Grid	0-1300m (131)	Below 1300m (10)

After visual inspection of the resulting field from each grid, the third grid was chosen as the appropriate one to continue (Figure 15). The first and the second grids, failed to retain the gradients of the field on the first and second transition depth respectively.

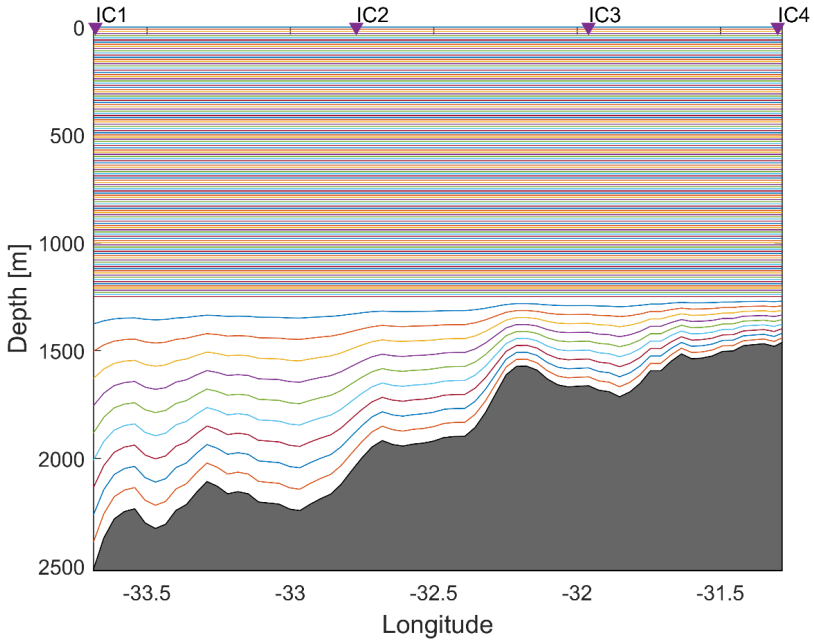

FIGURE 15: Schematic representation of the grid chosen (third) for the gridding of the velocity field on the whole section. Downward looking (purple) triangles indicate the position of the four moorings.

The chosen grid provides the flexibility to extrapolate the velocity field in the vertical and fill the whole basin. Special care should be taken for this process of extrapolation not to result in unrealistic values for the velocity. In each time step extrapolation was carried both towards the surface and towards the bottom topography. In our case, one can expect that the flow retains its strength or increases gradually towards the surface and that it retains its strength or decreases towards the bottom (Figure 14). In that manner, the velocity field was extrapolated using two methods: a) by keeping the last value closest to the bottom and closest to the surface constant to fill the gaps, and b) by extrapolating the velocity field using a gradient of 70 points (700m) close to the surface and of 3 points close to the bottom. This difference in the number of points used to determine the gradient, arose from the fact that the variability of the velocities is much higher in the upper part of the water column. Thus, a lot more values are required to get a solid representation of the evolution of the flow. The gradients' method makes more physical sense in our case (Figure 14) and was chosen to construct the velocity field and later calculate the volume transport for the whole section. In the final step, the new full depth profiles were spatially interpolated in the horizontal between subsequent mooring locations. Due to lack of: a) information about the expected shape of the oceanic phenomena described, b) sufficient correlation and c) physical boundaries, linear interpolation was performed. It is important to note that the same methods, described in this section, used for the velocity field were also used for the water mass characteristics.

3.2. Results: Directional Preference

In order to get an estimate of the directional preference of the velocity field daily, mean values of the north-south (v) and west-east component (u) of the velocity were used to calculate the standard deviational ellipses (SDE) of the velocity field depths down to 1000m in the water column. Standard deviational ellipses are the analogous of error bars in two dimensional space and represent the standard deviation along both axes simultaneously. The resulting ellipse for each individual time series used, captures the edge of one standard deviation (95% confidence interval) from the center of the data (mean) and the magnitudes of the ellipse axis, X and Y axis correspond to the u and v component of the velocity respectively, depend on the variance of the data. If the set of data points exhibits certain directional bias, there will be a direction with the maximum spread of the points, represented by the largest eigenvector of the covariance matrix of the data. In case that the distribution of the data is close to a multivariate Gaussian with zero covariance the major axis of the ellipse will be aligned with the normal axis. Otherwise the orientation of the ellipse will be at an angle Θ between the X axis and the largest eigenvector.

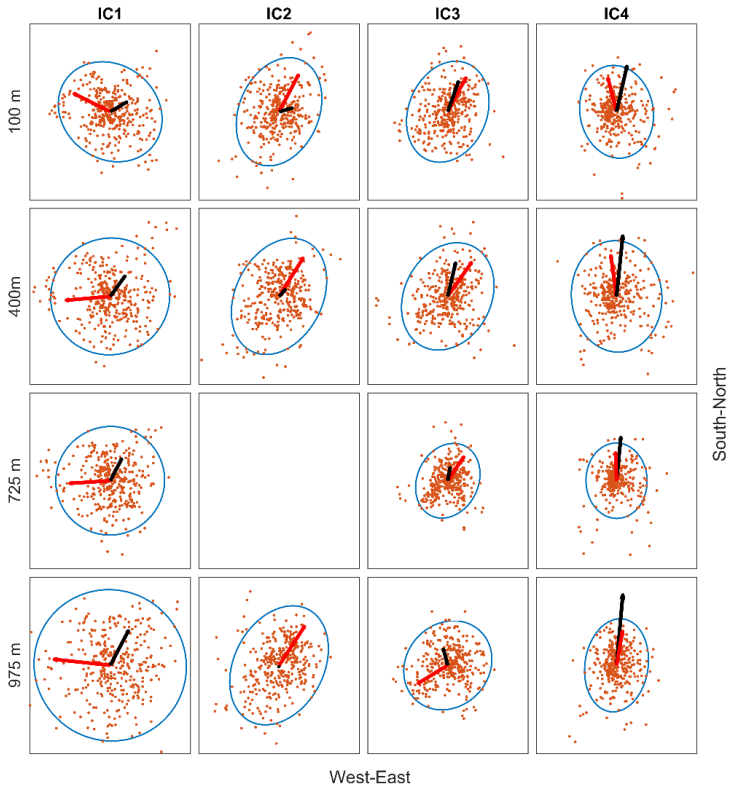

FIGURE 16: Demonstration of the directional preference of the velocity field at four depths (100m, 400m, 725m and 975m) up to 1000m on each mooring position (IC_1, IC_2, IC_3 and IC_4). Scattered brown points represent the data centered at (0,0), red arrows the largest eigenvector and black arrows the yearly mean velocity vector scaled by a factor of 4. The x and y axis have different limits, in order to retain the shape of each individual ellipse. Around 100m axis limits are between -0.6 m/s and 0.6 m/s, at 400m between -0.4 m/s and 0.4 m/s, at 725m between -0.3 m/s and 0.3 m/s and at 725m between -0.2 m/s and 0.2 m/s.

Standard deviational ellipses illustrated in Figure 16 provide various information of interest. At first one can notice changes in the magnitude of both the variance and the yearly mean velocity vector (black arrow) over the horizontal, between different moorings. On the one hand, in the upper 400m no significant differences are present between subsequent moorings, whereas below that depth the magnitude of variance grows from IC_4 (east) to IC_1 (west). On the other hand, the magnitude of the velocity vectors is high on IC_4 and low on IC_1, whereas in-between values are observed on IC_2 and IC_3. The magnitude of both variance and the yearly mean velocity vector decreases with depth on all mooring locations but that is not evident in Figure 16, due to the difference in the axis limits. The main feature of Figure 16 is the direction of the largest eigenvector (red arrow) that determines the orientation of the ellipses as follows:

- IC_1: The flow variance is largest to the West ($\pm$5°), with a minor deflection from the West axis of around 25°to the North at 100m.
- IC_2 and IC_3: Direction of the most variance is predominantly to the North-East, at an angle of $\sim 30 - 35$°to the East of the North axis, except on IC_3 at 975m where the orientation of the flow change from North-East to South-West.
- IC_4: The largest eigenvector is approximately to the North at all depths with an angle declination of $\pm$10°from the North axis.

In the horizontal it is evident that the orientation of the ellipses changes abruptly from Westward in IC_1, to North-Eastward in IC_2 and IC_3, to Northward in IC_4. This occurs at all depths apart the already mentioned exception of IC_3 at 975m depth where the orientation turns to the South-West. The above information apart from providing a first estimate of the variability of the flow both in the vertical and in the horizontal throughout the mooring line, serve as a guide for further analysis. Transport, in Chapter 4, needs to be calculated towards a certain direction but choosing an accurate direction to rotate the velocity field is not an easy task because of the large variability of its orientation. This is mainly due to the effect of the directional preference of the flow at the westernmost part of the line where the IC_1 is located. Nevertheless, the two components of the velocity were rotated 10°counterclockwise (-10°) to end up with the across and along section components of the flow. This was justified with the following arguments: a) It is a convenient rotation, as it matches the rotation applied to the two components of the hydrographically derived geostrophic velocity in Chapter 2 and allows for better comparison between them, and b) if we discard the effect of IC_1 on the direction of the flow this rotation is approximately the average rotation of IC_2, IC_3 and IC_4.

3.3. Results: Spectral analysis of across-section velocities

The purpose of the spectral analysis, is to detect dominant frequencies/periods of variability in the variable of choice. Here, daily across-section velocities along the mooring line and in depth at the position of each mooring were processed to produce the spectra of interest for this thesis. The most commonly applied technique to obtain the spectra out of a time series is the Fast Fourier Transform (FFT) which transforms the time series in the frequency domain (frequency and power). The data were prepared for FFT by subtracting the mean of each time series from its every point and by removing the linear trend (if any) from the whole dataset. Because the FFT is more effective when a time series has 2^n samples, every time series that currently contained 357 values was padded with zeroes to reach in length the next power of 2 which, for this case, is 512. A drawback of this padding is that it can introduce leakage (leak of variance from important to other frequencies) in the spectra since the gradient changes quickly to zero in the padded area in the end of the time series. This side-effect was minimized with the multiplication of a Blackman window with the data.

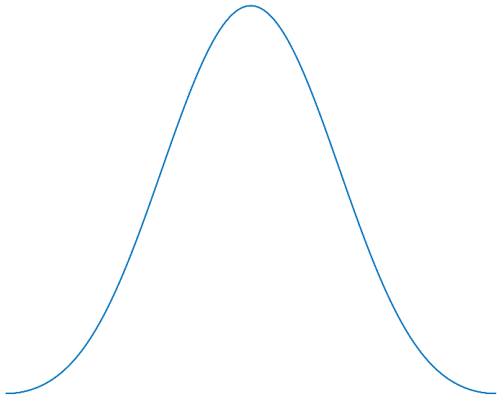

FIGURE 17: Blackman window that was applied to the zero-padded time series with length 512.

There are various methods that one can use for spectral analysis of time series though FFT. Thomson's Multitaper Method (TMM), described in a paper by Thomson (1982), offers an improved spectral estimate. It tries to address both leakage and variance using a combination of Finite Impulse Response (FIR) filters derived from a set of Slepian frequencies (discrete prolate spheroidal sequences). Furthermore, a time-bandwidth product n_w can be configured to change the number of tappers (windows) used to calculate the spectra and achieve balance between variance and resolution. This product is related to the number of tappers (n_t) through the following equation: $n_t = (n_w * 2)$–1. Increased n_w produces more estimates of the spectra and thus less variance, but at the same time more leakage as the bandwidth is also proportional to n_w. It is evident that the optimal time-bandwidth product is found through a process of trial and error and for this case it was chosen to be 1.5 producing 2 tappers in total. Finally, to resolve periodic behaviors, the presence of noise has to be taken in account. Time series should span at least a few repeat cycles with respect to the timescales analyzed. For the current nearly year-round time series, of 357 days, the maximum resolution chosen was 60-day periodic events (6 full cycles).

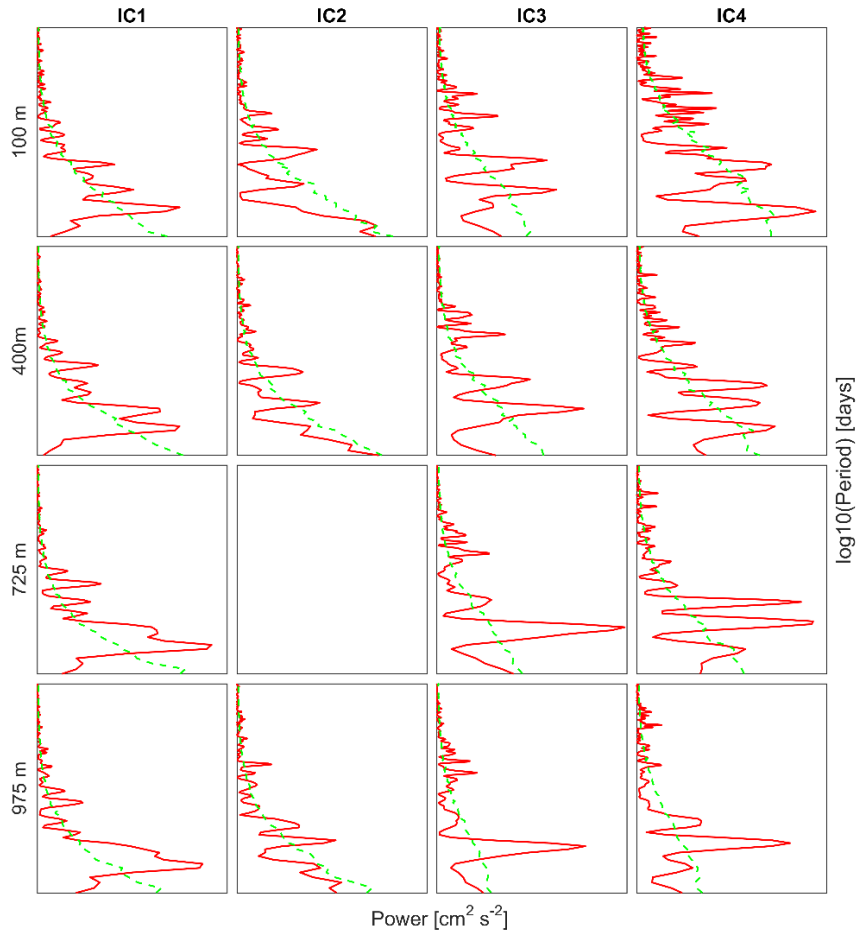

FIGURE 18: Power spectra (red lines) of the across-section velocities at four depths (100m, 400m, 725m and 975m) up to 1000m on each mooring position (IC_1, IC_2, IC_3 and IC_4). Green dashed lines represent the 95% confidence level which was calculated based on the confidence level derived from the analysis of multitaper (TMM) spectra from 1000 simulations of red noise, using a Monte-Carlo algorithm. A spectral peak is considered unreliable if it falls below the 95% confidence level.

Even though spectra presented in Figure 18 are relatively noisy, probably due to significant high frequency variability in this part of the upper ocean, one can notice common patterns in a close range of periods. These dominant periods fall into the mesoscale band with periods ranging from 7 ($\sim$ *weekly*) to 35 days ($\sim$ *monthly*). This is indicative of the importance of mesoscale variability in the Irminger Current.

TABLE 5: Dominant periods (in days) of the across-section velocities at four depths (100m, 400m, 725m and 975m) up to 1000m on each mooring position (IC_1, IC_2, IC_3 and IC_4).

	IC_1	IC_2	IC_3	IC_4
100 m	16.5, 24.5, 32	13.5	8, 15.5, 24.5	16.5, 34.5
400 m	12.5, 24.5, 32	13.5, 22	8, 15.5, 24.5	16.5, 22.5, 34.5
725 m	12.5, 24.5, 32		8, 15.5, 24.5	16.5, 22.5
975 m	12.5, 24.5, 32	7, 17.5, 22	8, 25.5	16.5, 22.5

3.4. Results: Monthly and seasonal changes

3.4.1. Changes in stratification and eddy activity

An excellent illustration of the buoyancy loss on the surface off the ocean during the winter of 2014-2015 is presented here. Figure 19, shows the collapse of the stratification in the upper 500m of the water column. The collapse is initiated during December 2014 and is evident in the section until early to late April 2015, depending on the mooring. For almost five months, the upper part of the ocean (500m) on top of each mooring was completely unstratified.

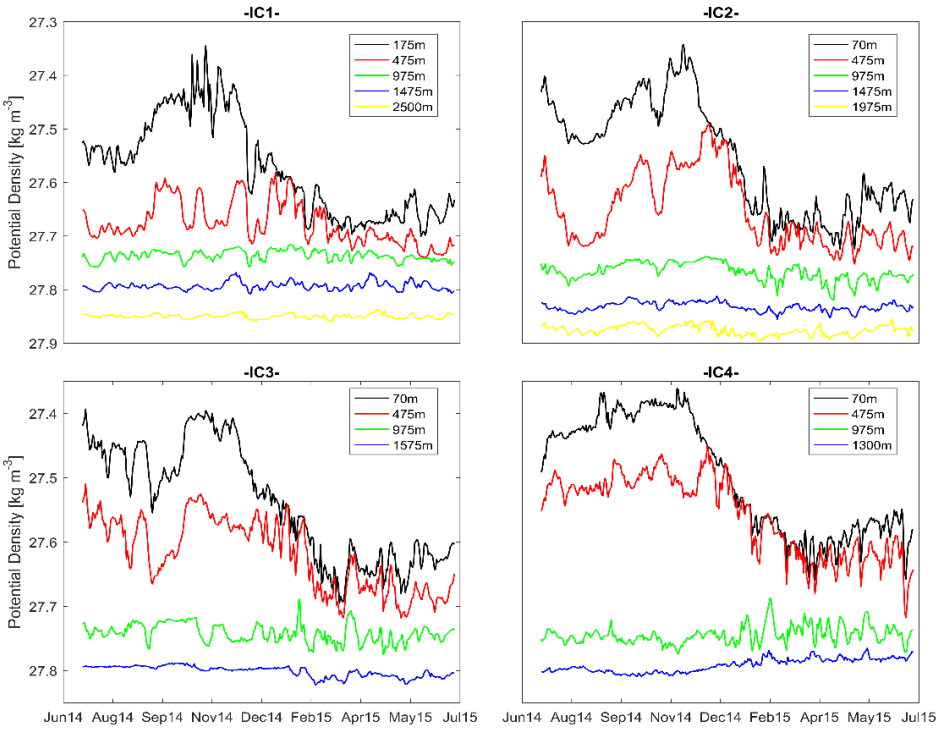

FIGURE 19: Potential density relative to the surface (σ_0) for the four moorings and for all available depths on each individual one. Note that potential density increases from top to bottom on the y axis of the plot.

Interestingly, this collapse, even though it happens at the same month, has a lag of some days from mooring to mooring. The density increase during the phase of the collapse is up to 0.25 kg m^{-3} which inevitably creates strong horizontal density gradients. This slumping of horizontal density gradients corresponds mostly to temperature gradients. Here, it could serve as a source for baroclinic instability and result in eddy generation. This could also be the case during April 2015, when heat loss from the ocean to the atmosphere ceased and restratification of the water column was initiated, again with a lag between adjacent moorings.

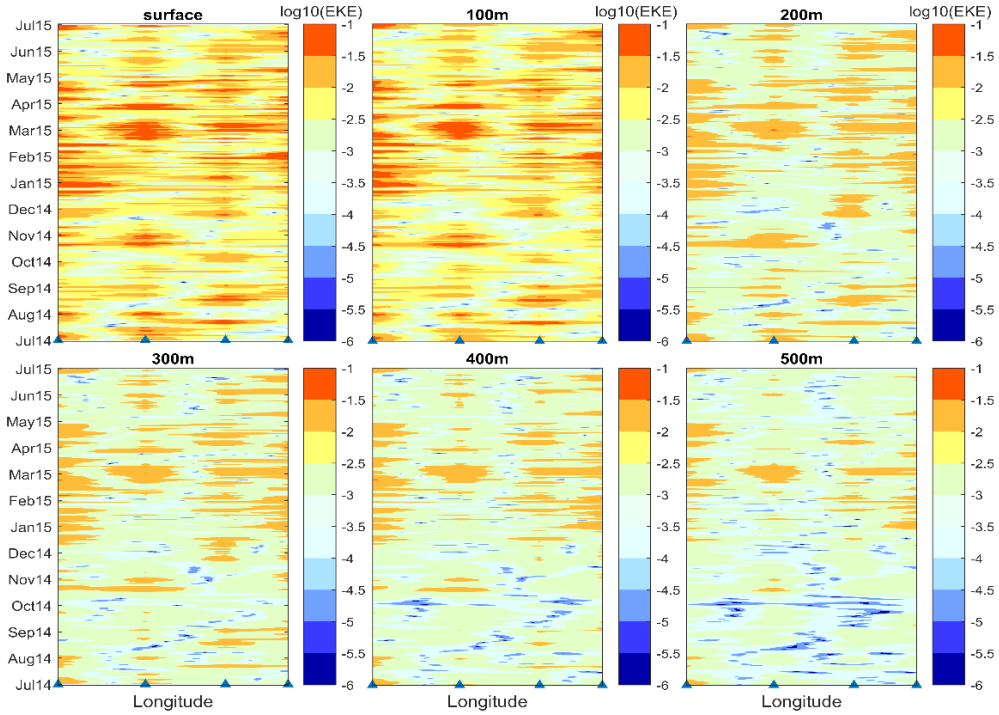

FIGURE 20: Hovmöller diagram of the base 10 logarithm of the Eddy Kinetic Energy (EKE) in the section, from July 2014 to July 2015. The EKE field is presented for 6 depths in the water column: a) surface, b) 100m, c) 200m, d) 300m, e) 400m, and f) 500m. Less negative values (hot colors) denote higher EKE and more negative values (cold colors) lower EKE.

Eddies can also be fed by shear in the mean flow, a process called dynamic instability. This way eddies gain their kinetic energy from the mean circulation. Thus, the world's oceans kinetic energy can be split into one associated with the mean flow and one related to the eddy component. The eddy constituent of the total kinetic energy field per unit mass was calculated for each grid bin using the following equation:

$$EKE = \frac{1}{2}[(u - \bar{u})^2 + (v - \bar{v})^2],$$

where u, v and $\bar{u}, \bar{v}$ signify the horizontal components of the velocity field in each bin of the grid at each time step and the yearly mean values of these components. The above Figure 20 shows that the EKE field in the section is very active particularly during the winter months. Although EKE is consistently high from mid-December 2014 to late-April 2015 at IC_1, the most concentrated high EKE values are observed from mid-February to mid-March 2015 at IC_2 mooring. The EKE decreases from the surface down to 500m in the whole section. Nevertheless, some eddy activity is still detected down to depths of 500m during the winter period. To wrap up, the section of interest displays the potential for the formation of mesoscale eddies through two different mechanisms: a) baroclinic instabilities, and b) dynamic instabilities. It is beyond of the scope of this study to investigate the eddy formation processes in more detail.

3.4.2. Monthly changes in conservative temperature

A way to understand year-round variations is to compare monthly mean fields of the variables of interest. This is how one can identify when and how changes took place. At first, monthly changes in conservative temperature are considered for the upper part of the water column (σ_0<27.7 kg m^{-3}). In depths, close to the 27.7 density contour temperature did not fluctuate much (4°C – 4.5°C). This density line signifies a barrier between a constantly evolving part of the ocean (upper part) and the rest of the ocean (lower part) where changes are much smaller. Throughout the course of the year (July 2014 – July 2015) the temperature field exhibited strong modifications close to the surface. In July 2014, temperature close to the surface ranged from minimum 5.5°C (IC_1) to maximum 7.5°C (IC_4). The next months (September – October 2014) temperature gradually increased over the whole section, after a slight decrease (0.5°C) close to IC_2 and slightly increase (0.5°C) close to IC_4 on August 2014.

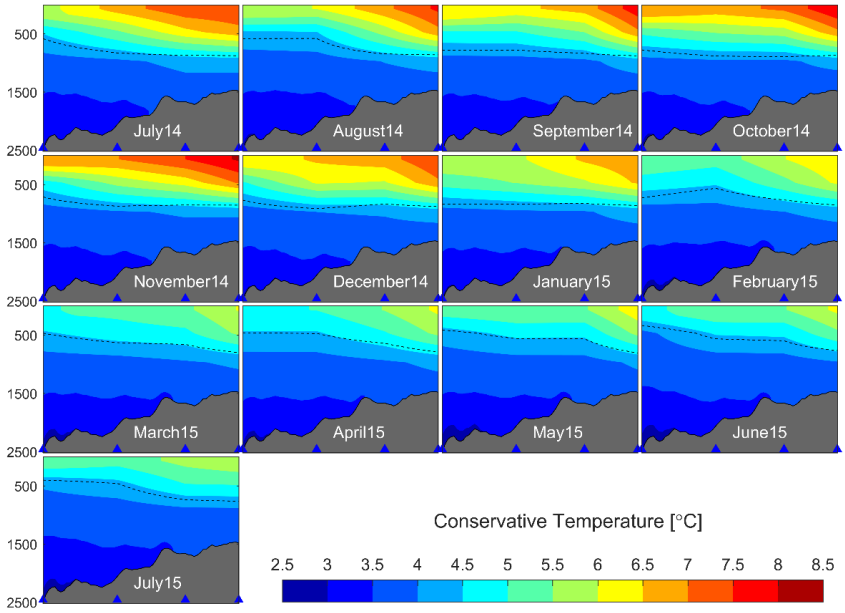

FIGURE 21: Conservative Temperature (°C) monthly means from July 2014 to July 2015. The black dashed line represents the monthly mean 27.7 kg m^{-3} density contour. Filled with blue color upward looking triangles denote the locations of the four moorings.

During November 2014, a slight increase of about 0.5°C was served, as warm waters spread westward from IC_4 up to IC_2. With the onset of winter, on December 2014, a section-wide decrease in temperature occurred with a rate of 0.5°C per month up to March 2015. The above is in agreement with the intense heat loss from the ocean to the atmosphere observed during the same period in the section. The following months (April – July 2015) the section displayed only small temperature fluctuations from March 2015. Thereby on July 2015 temperatures in the section ranged from minimum 5°C (IC_1) to maximum 6°C (IC_4), significantly lower than the previous July. Dynamical changes in the SG during periods of high atmospheric forcing (high NAO index) can result in eastward displacement of the North Atlantic Current (Flatau et al., 2003). Under this assumption, the Irminger Current as a branch of the NAC could also be displaced eastwards and thus delay the transport of warm and saline waters back to the Irminger basin.

3.4.3. Monthly changes in across-section velocities

In this part, monthly variations in the across-section velocities are discussed (Figure 22). The velocity field was highly variable and thus significant changes took place in monthly timescales. Special care should be taken while interpreting monthly mean velocities as the velocity field is also highly variable on smaller timescales. For the purpose of this chapter, the Irminger Current in the mean monthly fields, was identified from the following criteria: a) surface intensified flow, b) mean core velocities of at least 0.1 m s^{-1}, and c) spatial extend.

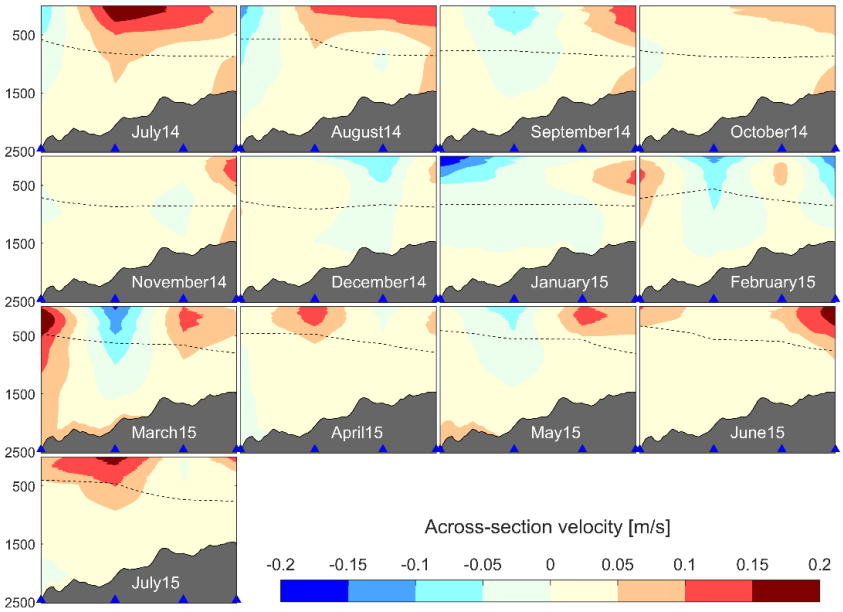

FIGURE 22: Across-section monthly mean velocities from July 2014 to July 2015. The black dashed line represents the monthly mean 27.7 kg m^{-3} density contour. Filled with blue color upward looking triangles denote the locations of the four moorings, which are (from east to west) IC_1, IC_2, IC_3 and IC_4.

In July 2014, the Irminger Current's spatial extend was from IC_2 to IC_3 mooring. Its core was found at IC_2 mooring, with maximum mean northward velocities that did not exceed 0.2 m s^{-1}, where the current also extends down to 1500m depth. The next month (August 2014) the current increased its spatial extend reaching IC_4 mooring. Core mean velocities of 0.15 m s^{-1} were spread in the mentioned locations but now the deep extension of the current, down to 1500m depth, moved to IC_4. For the following months of September and November 2014, the Irminger Current was located at IC_4 retaining its core velocities. During October 2014, the mean velocity field showed very weak structure with mean values that did not exceed 0.1 m s^{-1}. With the onset of winter (December 2014) the variability increased significantly and up until February 2015 the across-section flow on the section was weakly northward or even southward. It seems that during this period the current was pushed outside the area of measurements. On March 2015, the Irminger Current suddenly appeared at IC_1 mooring, having regained maximum mean core velocities of 0.2 m s^{-1}, and was extending all the way down to the bottom in a depth of 2500m. The same month, the mean flow was southward at IC_2 and northward at IC_3 with a weak core

located around 200m depth. This observed feature was extending down to 750m in both locations and it could be an oceanic eddy, although a clear conclusion cannot be drawn from the velocity field alone. From April 2015 and up till July 2015, variability decreased in comparison with winter time. The Irminger Current meandered between IC_2, IC_3 and IC_4, gradually regained its strength in core velocities up to 0.2 m s^{-1}, and ended up at IC_2 mooring on July 2015. This is the same location that the current was found in July 2014. However, then it was slightly stronger and had more vertical extend. It is crucial to note that at many points in time, it seems that the mooring line captures half or less of the mean core flow of the Irminger Current. This is mostly evident in the easternmost mooring of the section (IC_4) for example in September 2014, November 2014, June 2015, whereas on the westernmost mooring (IC_1) it is observed once on March 2015. This issue concerns the resolution of the moorings and will also be examined in the following chapters. In general, these first year-round data show that the Irminger Current is highly variable in space and time, particularly during the winter.

3.4.4. Seasonal changes

The monthly mean across-section field demonstrated significant variability, particularly during winter months. This is presented here more explicitly with the seasonal variability. As it is the first time that changes in the velocity field are captured during the winter in this section, it is of great importance to highlight the seasonal differences of the flow there. The year-round monthly mean daily across-section velocity field, was averaged and split into three periods: a) Summer to Autumn (July - November 2014), b) Winter (December 2014 -March 2015) and c) Spring to Summer (April - July 2015). The results shown in Figure 23 are remarkable. The mean flow during the first period (July – November 2014) is strongly northward. Significant mean northward flow extends from IC_2 to IC_4 in the upper 500m, and the core velocities are located at IC_4 where the flow extends down to depths of 1500m. The situation is very similar for the third period (April – July 2015) again, were northward flow is apparent section-wide in the upper 500m. Core velocities, and subsequently the Irminger Current, are again found on top of IC_4 mooring where the flow similarly extends down to depths of 1500m. Up till now, the notion was that the flow in the area is northward throughout the year, a picture obtained mainly by data from summer hydrographic sections. Indeed, if one considers the situation described in Chapter 2, where the absolute geostrophic field is presented for summer 2014 and 2015, one can conclude that the flow is predominantly to the north throughout the seasons. This picture is shattered into pieces, looking into the above mean across-section velocity field for the winter of 2014-2015 (December 2014 – March 2015). Surprisingly, the mean flow is strongly to the south with core velocities concentrated on top of IC_2 mooring and reaching down to depths of 1500m. It is unclear if this situation represents a regular seasonal cycle, never recorded before, or if it is a consequence of the high atmospheric forcing and the subsequent deep convection that took place this winter. Longer time series are needed to answer this kind of questions.

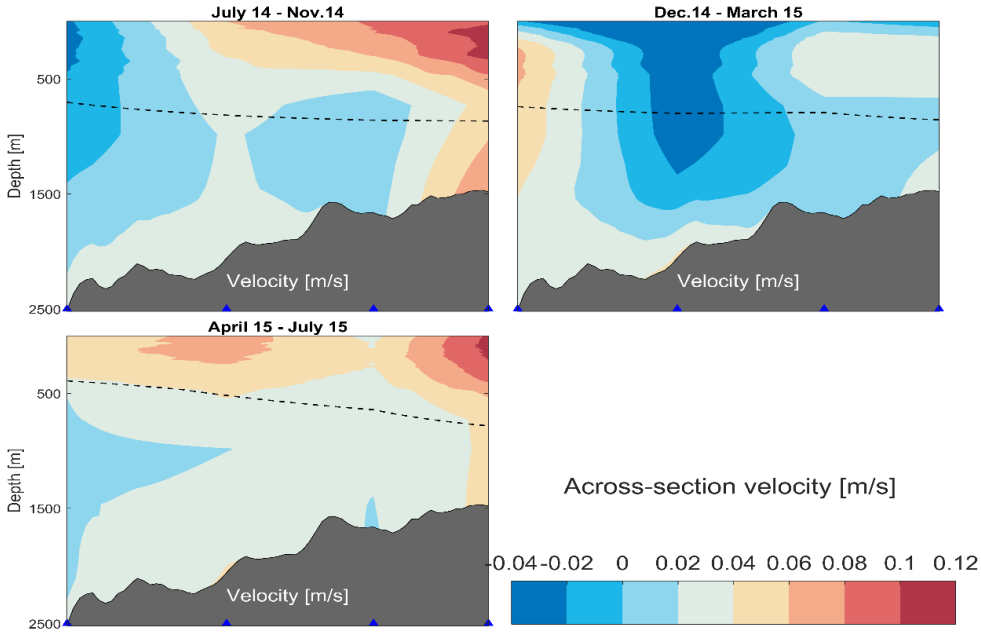

FIGURE 23: Illustration of seasonal variations in the section of interest. Across-section velocities (m s^{-1}) were averaged into three periods: Summer to Autumn (upper left), winter (upper right) and spring to summer (lower left). The black dashed line represents the 27.7 kg m^{-3} density line and blue upward looking triangles the four (4) moorings namely, from west to east, IC_1, IC_2, IC_3, IC_4.

Another difference that arose from the above Figure 23, is the difference in the mean seasonal gradient of the 27.7 kg m^{-3} density line across the section. During the first period, there is a week mean density gradient, positive from west (IC_1) to east (IC_4). This gradient is diminished in the second period, although this is most probably an artifact of averaging. Moreover, the fact that the mean gradient is very close to zero (0) is a result of averaging intense positive and negative gradient fluctuations that are evident in shorter time scales and constitute a sign of strong mesoscale activity. In the last period, where fluctuations are not so extreme, a strong positive density gradient is apparent and showcases the effect of buoyancy loss during winter time, that was more prominent on the western side of the section. Lastly, the idea that the spatial resolution of the mooring is not sufficient to capture the Irminger Current is again confirmed from these seasonal across-section velocity fields.

Chapter 4 - Results: Volume Transport

The Irminger Current transports warm and saline waters of Atlantic origin to the Irminger basin. Documenting the volume transport of these waters in time, is essential in order to understand changes in the Subpolar Gyre and to a greater extend changes in the Atlantic Meridional Overturning Circulation. In this Chapter, we investigate the evolution in time of the total net volume transport in the section (TNVT) and of the volume transport of the Irminger Current. Then, all the available estimates of the northward transport are compared with literature, and with the output of an eddy resolving model.

4.1. Total net volume transport

The time series of the total net volume transport (TVNT) for the section, in Sverdrup (1 Sv=$10^{-6}m^3s^{-1}$), was calculated from the integral of the across-section velocity field over the area of the section $\iint V_{as}\, dz\, dl$ where V_{as} is the across section velocity,z the depth and l the horizontal distance. As this is the first time we have full depth year-round measurements in the section, it is interesting to first take a look at the evolution of the direction of the section-wide flow throughout this year there.

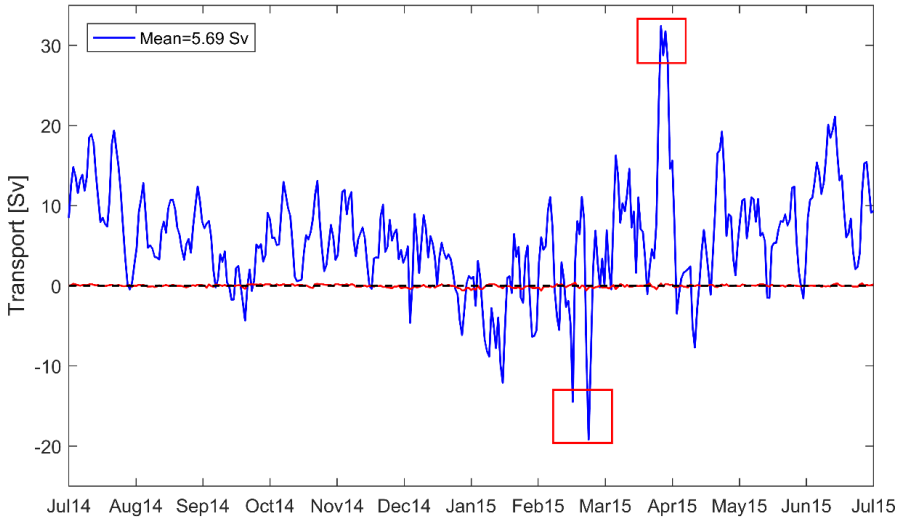

FIGURE 24: Year-round total net volume transport (Sv) for the whole section. Positive values indicate northward and negative values southward transport across the section. The yearly mean value of the transport in noted in the legend. The red line illustrates the difference in transport between the two extrapolation methods (section 3.1.1.3) used to calculate the velocity field.Finally, red boxes enclose a set of peaks that are of interest here.

The total net volume transport time series (Figure 24) exhibits high variability even in daily basis. Throughout the year, values of the TVNT ranged from -20 to +32 Sv. From a first look, it seems that fluctuations in the transport are more significant during the winter than the rest of the year. The yearly mean value of the TVNT daily transport time series (T_{daily}) is 5.69 Sv, with a standard deviation (std) of 6.66 Sv about the mean. The error of the mean transport was calculated with the following equation: $T_{error} = \frac{std(T_{daily})}{\sqrt{N_{eff}}}$, where

$N_{eff} = \frac{N}{n_d}$ is the effective number of degrees of freedom on the estimated uncertainty, N is the number of observations and n_d is the number of degrees of freedom in the set of measurements. Visual inspection of the autocorrelation function of the TVNT daily transport time series showed that decorrelation of the measurements takes place at lag 57. Thus n_d=57 and T_error= 2.66 Sv which finally leads to a yearly mean value of 5.69±2.66 Sv for the TVNT daily transport time series.

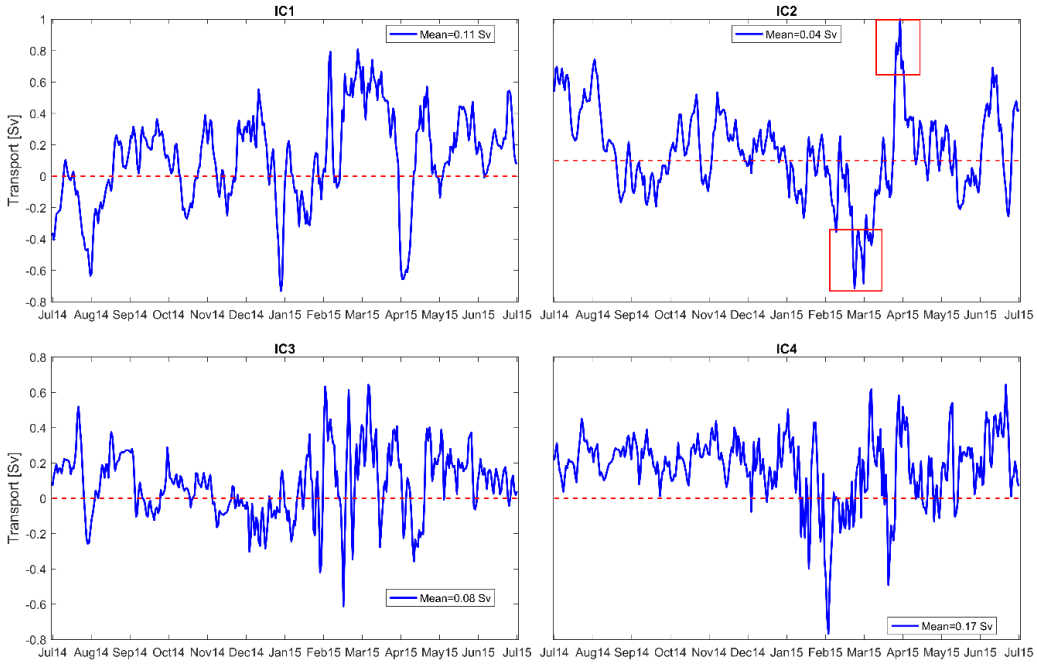

FIGURE 25: Total net volume transport for the four moorings on the section. The transport for each mooring was calculated from the vertical profile of the velocity field on the horizontal grid bin assigned to it. Positive values indicate northward and negative values southward transport across the section. The yearly mean value of the transport in noted in the legend. Red boxes on the top right panel enclose a set of peaks that are of interest here.

Maximum southward transport (-15 to -20 Sv) occurred in late-February 2015 (Figure 24) when a strong southward flow, extending down to 1500m depth, was present mainly at IC_2 mooring (Figure 14). Maximum northward transport (+32Sv) occurred during late-March to early April 2015 (Figure 24), when a strong northward flow was apparent, mainly on top of IC_2 mooring. The core of this flow was found on the upper 500m but for the most part it was extending down to depths of 1000-1500m (Figure 14). To examine the origin of those extremes the transport time series was split according to frequency bands that were determined through inspection of the power spectra (spectra computed as in section 3.3).

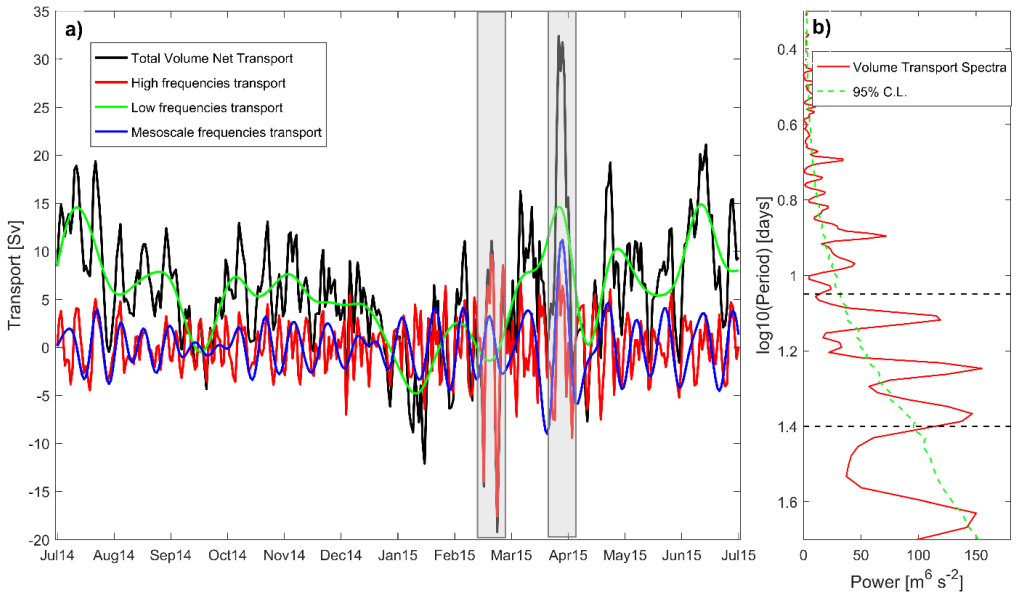

FIGURE 26: a) Total Net Volume Transport (TVNT) time series decomposed according to three frequency bands: i) high frequencies transport (red line), ii) mesoscale frequencies transport (green line) and iii) low frequencies transport (blue line). The original transport time series is show by the black solid line and its large peaks are shaded with light grey color. b) Power spectra (red line) of the volume transport of the Irminger Current. Green dashed lines represent the 95% confidence level which was calculated based on the confidence level derived from the analysis of Multitaper (TMM) spectra from 1000 simulations of red noise, using a Monte-Carlo algorithm. A spectral peak is considered unreliable if it falls below the 95% confidence level. Black dashed lines enclose the mesoscale band of periods of interest here.

The most energy in the spectra lies in a mesoscale band of periods, with dominant peaks at 13,18 and 24 days (Figure 26, panel b). Thus, the original transport time series was decomposed into three time series, corresponding to three different frequency bands, by filtering in the frequency domain (Figure 26, panel a): a) High frequencies transport - time series of transport derived by filtering from the original time series frequencies lower than $\frac{1}{12}$ days using a Butterworth high pass filter, b) Mesoscale frequencies transport – time series of transport derived after the application of a Butterworth bandpass filter to the original time series allowing only frequencies between $\frac{1}{12}$ to $\frac{1}{25}$ days, and c) Low frequencies transport – time series of transport derived by filtering from the original time series frequencies higher than $\frac{1}{25}$ days using a Butterworth low pass filter. All these subseries of transport add up to the original transport time series. This process demonstrates that the highly negative peaks of the transport (Figure 26, panel a, shaded grey area on the left) are attributed to high frequency variability. The large positive peak (Figure 26,panel a, shaded grey area on the right) was fed from all the bands but particularly the low frequency (contribution of 15 Sv) and the mesoscale one (contribution of 12 Sv). In general, the most transport is accredited to the low frequency band with a mean value of 5.63 Sv, with mesoscale and low frequency ones having mean values of 0.04 Sv and 0.02 Sv respectively.

4.2. Volume Transport of the Irminger Current

The volume transport of the Irminger Current was calculated as in the previous section but only from the positive values of the across-section velocity field. In the context of this chapter we have assumed that all the northward transport in the section is part of the Irminger Current. Other oceanic phenomena (e.g. eddies) that cause water to move northward are also active in the section but it was not on the scope of this report to quantify them.

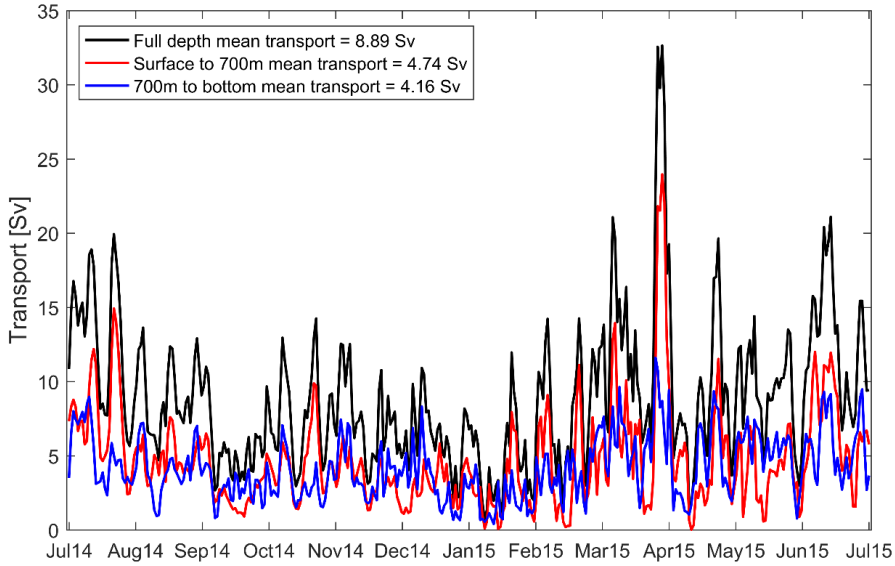

FIGURE 27: Illustration of the northward volume transport in the section, representing the transport of the Irminger Current (Sv). Full depth, surface to 700m and 700m to bottom transport is represented with solid black, red and blue line respectively.

The volume transport time series of the Irminger Current (Figure 27) exhibits similar high daily variability as the TNVT presented in the previous section. The yearly mean value is 8.89 Sv, with a standard deviation (std) of 4.84 Sv about the mean. The error of the mean transport was calculated as in the previous section (decorrelation lag of 42 days) and was found to be 1.66 Sv. The mean transport decreased $\sim$ 2 Sv from the summer-autumn period in 2014 to the winter of 2014-2015 but then increased $\sim$ 3 Sv during the spring-summer period in2015, in part due to the peak around late-March. Apart from the major peak, already mentioned in the previous section (value of 32 Sv), there seems to be an upper limit in the transport with other peaks not exceeding a value of $\sim$ 20 Sv. The Irminger Current is expected to have a surface intensified flow and this is most certainly shown in Figure 27. For the purposes of this section we split the full depth transport into upper and lower transport, denoting the transport from the surface down 700m depth and from 700m depth down to the bottom of the ocean respectively.

Even though the mean upper and lower transports are close (4.74 and 4.16 Sv), there is a major difference between them. The variability is by far larger in the upper one and the majority of the peaks above the mean in transport, are caused by variability in the upper part of the water column. Nevertheless, there are many cases that both parts of the ocean (upper and lower layer) equally contribute to the total transport which is an indication of a deep extension of the Irminger Current.

4.3. Comparison of northward volume transport estimates

In order to facilitate differences between current and previous estimates of the northward volume transport of the Irminger Current, a comparison is essential. In that manner, the transport estimate from this Chapter is compared with the geostrophic transport estimates from Chapter 2 ,with model output and with the transport estimates from Våge et al., (2011). The latter were obtained from hydrography and SSH only.

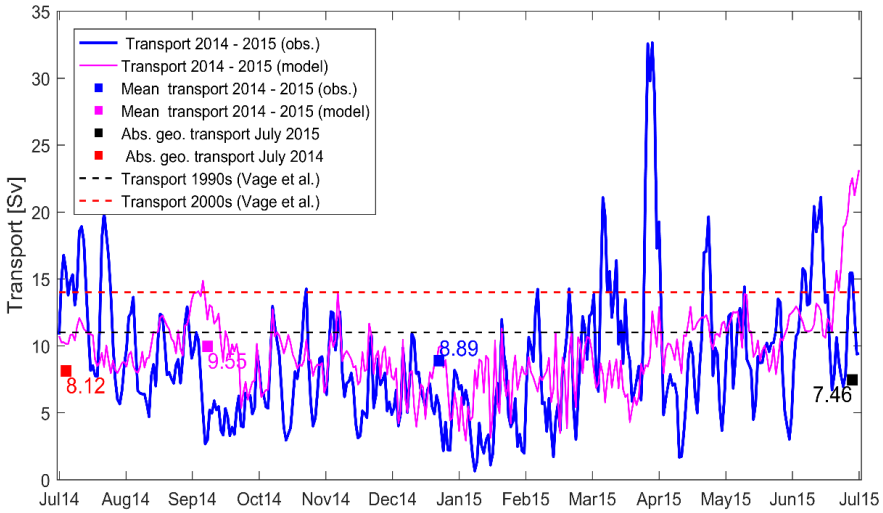

FIGURE 28: Comparison between different estimates of the Irminger Current transport. Blue and magenta solid lines represent the year-round transport time series for the section derived from observations (Chapter 3) and the model output respectively. Black and red dashed lines denote the mean transport of the current in the 1990s (1990-1994) and in the 2000s (2000-2004).

In spite of the variability of the current throughout the year, there is a fairly good agreement between the hydrographic estimates from the July 2014 and July 2015 (8.12 Sv and 7.46 Sv) and the mean transport of the Irminger Current derived from year-round mooring data (8.89 Sv.). Differences are within the error limits and could also be attributed to the fact that the geostrophic transport is only a part and not representative of the full transport captured by the moorings. Comparison between the 1990s and July 2015 (high NAO index) and between the 2000s and July 2014 (low NAO index) results in a difference of around 6 Sv and 3.5 Sv respectively, similar to the difference with the yearly mean transport of 2014-2015 (8.89 Sv). Våge's mean estimates for the 1990s (11 Sv for 1990-1994) and the 2000s (14 Sv for 2000-2014) were based on a combination of hydrographic and satellite data and resulting errors for some years were as large as 10 Sv.

Additionally, inter-annual variations in the transport during these periods were similarly high as the daily variations shown here (Chapter 3). The above could partly justify the difference with Våge's estimates. This discrepancy could also be explained from the fact that: a) the northward winter time flow is weak in the section (Chapter 3) and b) at many cases it seems that the mooring line does not fully capture the northward flow of the Irminger Current (Chapter 3 and 4). It could be the case that Våge overestimated and we underestimated the transport of the Irminger Current.

In order to shed more light on the above comparison, the northward transport for the section was also calculated using the output of an eddy resolving global ocean model freely available online (http://marine.copernicus.eu/). The resolution of this model is $\frac{1}{12}$ of a degree($\sim$ 8km) and is forced with ECMWF data. The model exhibits significantly less variability in the transport than the observations, having a mean value of 9.55$\pm$1.39 Sv and a standard deviation of 2.93 Sv around the mean. Even though the model fails in representing the fluctuations in the daily transport time series, it fairly well captures the yearly mean northward transport in the section. The disagreement between the model and the observations (0.66 Sv) is not significant, considering that the error estimates for both are greater than this number. Additionally, this value falls in the middle of the estimates obtained from Våge (absolute geostrophic transport 1990s) and from year-round observations (2014-2015), Figure 28.

Chapter 5 - Results: Mean Absolute Dynamic Topography

Absolute dynamic topography (ADT) is the sea level above the geoid (ocean at rest), through which the world's ocean circulation features, like gyres and currents, can be derived using the geostrophic approximation. Altimetric satellites measure sea level variations (SSH) above the ellipsoid which are then used to calculate ADT with the following equation: ADT=SSH-GH, where GH is the geoid height. Daily mean gridded ADT (MADT) for the Irminger basin extracted from the AVISO MADT (all sat merged, $\frac{1}{4}x\frac{1}{4}$ resolution in degrees, on a Cartesian grid) dataset is tested here as to whether it can be used to understand lateral changes in the water movement on the section, and on a broader scale in the Irminger basin. As high resolution altimetric data are now available, it is interesting to ask if there is a connection between absolute dynamic topography (ADT) along and the meridional transport across a zonal section like ours.

In that manner, we first compared various transport time series from Chapter 4 with the MADT product in order to find similarities between them based on correlation methods. Satisfactory agreement was found between the meridional low frequency northward transport (derived as the total net low frequency northward transport (LFNT) in section 4.1) and the zonal MADT gradient in the section. This gradient was calculated from the difference in the MADT field between the east bin of the easternmost (IC_4) and the west bin of the westernmost (IC_1) mooring in the section. The correlation between the time series was characterized from a correlation coefficient of 0.50 and was significant in the 95% confidence intervals (p value of 0.01).

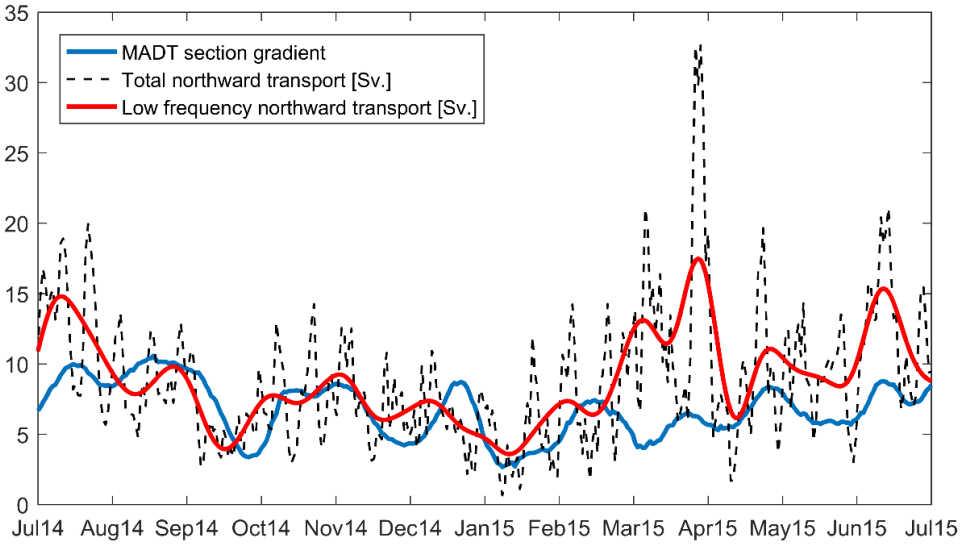

FIGURE 29: Illustration of the zonal MADT gradient (solid blue line) along with total northward (black dashed line) and low frequency northward (solid red line) transport in the section. Correlation between the MADT gradient and the total and low frequency transport is 0.25 and 0.50 respectively and is significant in the 95% confidence intervals.

Qualitatively the MADT gradient performs fairly well in illustrating the evolution of the low frequency northward transport (LFNT) in the section (Figure 29). Even though the large peaks in LFNT (particularly in April 2015) were not captured by the MADT gradient, in most cases peaks of the gradient follow those of the LFNT with a delay of some days. Additionally, the LFNT yearly mean value is 8.85 Sv, almost the same as the yearly mean value of the total northward transport which is 8.89 Sv. Taking in account the above, we could conclude that the MADT field could potentially be used to estimate the northward transport in the section. It should be kept in mind though that the Irminger Current itself is likely undersampled and that not all of its transport is captured (i.e. east). More sophisticated approaches should be developed that will enable us to us MADT for proxy for transport estimates. Although qualitatively is shown here to be possible, it was not in the scope of this study to investigate this in detail.

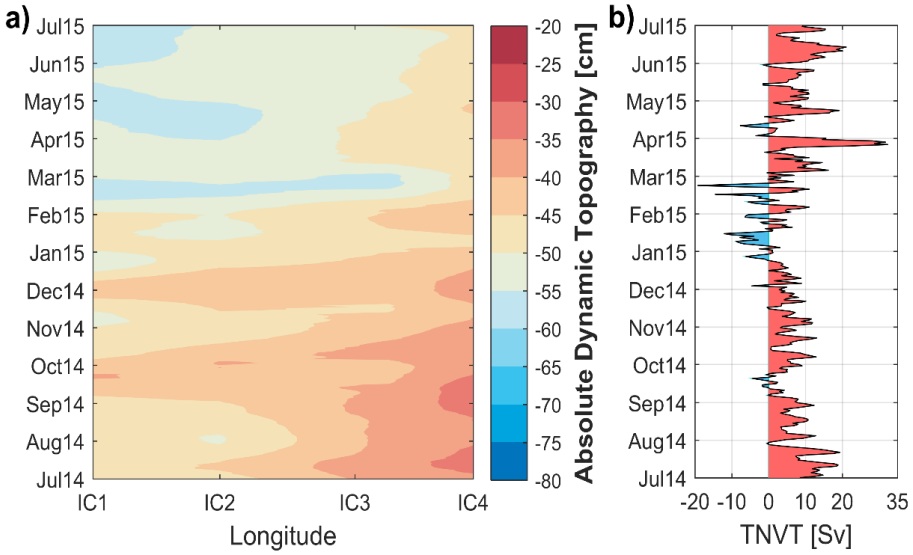

FIGURE 30: a) Hovmöller diagram of the mean absolute dynamic topography (MADT) in the section from July 2014 to July 2015. Red values indicate higher MADT/SSH values than blue ones. b) Total net volume transport in the section from July 2014 to July 2015. Red and blue colored areas denote positive (northward) and negative (southward) transport respectively.

Another way to look at it, is by comparing the evolution in space and time of the MADT field (Hovmöller diagram) with the total net volume transport in the section (Figure 30). One the one hand, changes in the volume transport at many points in time are evident with a time lag of some days in the MADT. During mid-to-late July 2014 the volume transport decreased abruptly and then recovered during the first days of August 2014. These changes were reflected in the MADT, where a decrease during early-to-mid August 2014 and an increase back to the same values was observed close to IC_4 mooring. The above was likely due to a temporally eastward displacement of the Irminger Current. A shift of the transport to mostly negative values (southward direction) was documented during the winter of 2014-2015. Basin-wide decrease in the MADT field during this period, likely induced the Irminger Current to move eastward and out of the range of the mooring array.

On the other hand, some features of the transport were not detected in the MADT. For example, the highly positive peak (northward direction) in the transport during late March 2015 was not seen at all in the MADT. This is likely due to the fact that this peak was partly caused by mesoscale activity in the section (section 4.1, Figure 26, panel a). The gridded AVISO product used in this chapter filters eddies with spatial extend less than 40km (Chelton et al., 2011), while a study in the Irminger Sea have shown that eddies there do not exceed this length in diameter (Fan et al., 2013). Hence, these eddies are not captured by the MADT field but they have major impact on the transport we obtained.

Generally, during this one-year period MADT is larger in the eastern than in the western side of the section with maximum values consistently observed closer to the easternmost mooring (IC_4), (Figure 30). This indicates that the Irminger Current, expected to be found in the section, is likely mostly located in the eastern part of the section close to the Reykjanes Ridge. From July to the beginning of September 2014, MADT was in general lower in the west than in the east of the section with maximum values of -30cm observed close to IC_4 mooring. Then during the next month, MADT slightly increased in the western and decreased in the eastern side of the section. This was followed by slight section-wide decrease and then increase until the end of November 2014 and mid-December respectively. After these periods, another section-wide decrease in the MADT took pace until the beginning of February 2015 when MADT dropped precipitously in the whole section reaching minimum values of -60cm. Values of MADT dropped as much as 15cm in less than 2 weeks. After this drop and up until July 2015, MADT values: a) west of IC_3 fluctuated closely to the minimum of February 2015, and b) east of IC_3 slightly increased. Throughout this one year, MADT showed a section-wide decrease of about 15cm and did not return to the values of July 2014.

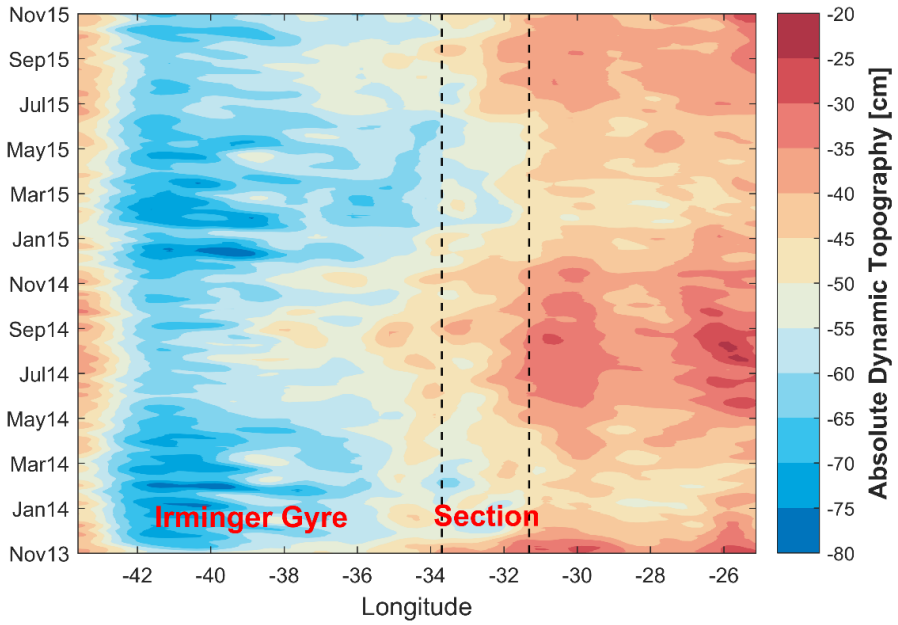

FIGURE 31: Hovmöller diagram of the mean absolute dynamic topography (MADT) in the Irminger basin from November 2013 to November 2015. Red values indicate higher MADT/SSH than blue ones.

This return, happened one month later in August 2015 than in 2014 and is shown in Figure 31. Additionally, this event was in accordance with broad changes than took place in the Irminger basin. Figure 31 illustrates that during the winter of 2014-2015 low MADT values were pushed a lot closer to the section than the previous winter and remained there almost until July 2015. Additionally, high MADT values on the east of the section decreased significantly over the course of the winter. Even though an increase started in the beginning of July 2015, high MADT values as the ones observed during the summer of 2014 were not recovered. This is likely a sign that the whole Subpolar Gyre expanded to the east during the winter of 2014-2015 and did not return to its previous state.

Chapter 6 - Conclusions and recommendations

6.1. Summary and conclusions

Significant changes took place in the Irminger Sea during the winter of 2014-2015, conversely analogous to the ones described in Våge et.al (2011) from the early 1990s to the early 2000s. High atmospheric forcing (high NAO index), resulted in highly positive wind stress curl and anomalously high heat loss in the area. Analyzing hydrographic data from two transects (July 2014 and 2015) at $\sim 60°$N across the Irminger basin, we concluded that deep convection occurred inside the Irminger Gyre and that Labrador Sea Water was locally formed. In summer 2015, the absolute geostrophic field exhibited a single core for the Irminger Current, similar to the summer state of the 1990s. Then, we examined the first year-round results from a full depth mooring array located on the west side of the Reykjanes Ridge between July 2014 and July 2015. The Irminger Current was found to be much more variable than earlier thought, even in daily basis. Monthly and seasonal mean fields revealed the abrupt changes that happened on the section during wintertime (December 2014 – March 2015). Mean conservative temperature in the upper 500m of the water column plummeted $\sim 2°$C and the mean flow was (remarkably) to the south. Clear conclusions could not be made as to whether and by how much this wintertime variability is part of a regular seasonal cycle and/or was a result of the deep convection observed in the basin during the same period. Additionally, the Irminger Current was mostly located close to the IC4 mooring and was found to transport of 8.89 ± 1.66 Sv in an annual mean sense. Even though our estimate was lower than the previous ones from Våge et al. (2011), it was in good agreement with our geostrophic transports for the summer periods and the model's transport. Both mesoscale and high frequency activity were found to strongly contribute to large peaks of the net volume transport in the section. Investigation of the mean Absolute Dynamic Topography in the section led to the conclusion that this field could theoretically be used to roughly estimate the transport of the Irminger Current. Moreover, together with earlier results, the MADT field hinted to an expanded Subpolar Gyre as of winter, 2015. Finally, the spatial resolution of the moorings was found to be likely too coarse to capture the full transport of the Irminger Current. This was supported by a combination of observations and model output (see also Figure 33, Appendix).

6.2. Recommendations for further study

1. As this study was based on a short (one year) time series, the complete OSNAP time series of four years (2014-2018) will allow future research on the Irminger Current to be conducted more in depth. Longer time series will provide a more complete picture for the magnitude and the source/s of variability. It will also enable us to determine if wintertime variability in the section is part of a regular seasonal cycle or/and a consequence of local convection events. To quantify the effect of convection on the Irminger Current and in a bigger scale on the Subpolar Gyre will also contribute in the improvement of present model's representation of oceanic variability.

2. The horizontal spatial extend of the moorings, likely did not allow us to capture the full transport of the Irminger Current. Additionally, the distance between individual moorings ($\sim$ 40km) is greater than the diameter of a typical eddy in the Irminger basin. Thus, these mesoscale phenomena cannot be extensively studied. A French mooring array, was placed on both sides of the Reykjanes Ridge during the summer of 2015; with the recovery scheduled for summer 2017. The French moorings in our section were placed in-between our moorings. Merging of the full OSNAP time series (2014-2018) with these measurements as well as data from an American mooring, also located on the east side of the ridge, will hopefully resolve these issues.

3. The mean Absolute Dynamic Topography has the potential to be used as a way to estimate the transport of the Irminger Current from altimetric data. However, this should first be complemented still with in-situ data, ideally time series from a combination of core moorings. These can be identified after the study suggestion in point 2. Further research is essential on this topic, specifically to reduce the large costs of an array in the future. Special care should be given for the construction of an index. For this to be possible non-geostrophic contributions to the transport in the section must first be understood and accounted for.

Bibliography

[1] Barrier, N., Cassou, C., Deshayes, J., & Treguier, A. M. (2014). Response of North Atlantic Ocean circulation to atmospheric weather regimes. *Journal of Physical Oceanography*, 44(1), 179-201.

[2] Bersch, M., Yashayaev, I., & Koltermann, K. P. (2007). Recent changes of the thermohaline circulation in the subpolar North Atlantic. *Ocean Dynamics*, 57(3), 223-235.

[3] Chelton, D. B., Schlax, M. G., & Samelson, R. M. (2011). Global observations of nonlinear mesoscale eddies. *Progress in Oceanography*, 91(2), 167-216.

[4] Corbière, A., Metzl, N., Reverdin, G., Brunet, C., & Takahashi, T. (2007). Interannual and decadal variability of the oceanic carbon sink in the North Atlantic subpolar gyre. *Tellus B*, 59(2), 168-178.

[5] Daniault, N., Mercier, H., Lherminier, P., Sarafanov, A., Falina, A., Zunino, P.,& Thierry, V. (2016). The northern North Atlantic Ocean mean circulation in the early 21st century. *Progress in Oceanography*, 146, 142-158.

[6] De Jong, M. F., Drijfhout, S. S., Hazeleger, W., Van Aken, H. M., & Severijns, C. A. (2009). Simulations of hydrographic properties in the northwestern North Atlantic Ocean in coupled climate models. *Journal of Climate*, 22(7), 1767-1786.

[7] De Jong, M. F., & Steur, L. (2016). Strong winter cooling over the Irminger Sea in winter 2014–2015, exceptional deep convection, and the emergence of anomalously low SST. *Geophysical Research Letters*, 43(13), 7106-7113.

[8] De Jong, M. F., van Aken, H. M., Våge, K., & Pickart, R. S. (2012). Convective mixing in the central Irminger Sea: 2002–2010. *Deep Sea Research Part I: Oceanographic Research Papers*, 63, 36-51.

[9] Doyle, J. D., & Shapiro, M. A. (1999). Flow response to large-scale topography: The Greenland tip jet. *Tellus A*, 51(5), 728-748.

[10] Fan, X., Send, U., Testor, P., Karstensen, J., & Lherminier, P. (2013). Observations of Irminger Sea anticyclonic eddies. *Journal of Physical Oceanography*, 43(4), 805-823.

[11] Flatau, M. K., Talley, L., & Niiler, P. P. (2003). The North Atlantic Oscillation, surface current velocities, and SST changes in the subpolar North Atlantic. *Journal of Climate*, 16(14), 2355-2369.

[12] Häkkinen, S., & Rhines, P. B. (2004). Decline of subpolar North Atlantic circulation during the 1990s. *Science*, 304(5670), 555-559.

[13] Halloran, P. R., Booth, B. B. B., Jones, C. D., Lambert, F. H., McNeall, D. J., Totterdell, I. J., & Völker, C. (2015). *The mechanisms of North Atlantic CO2 uptake in a large Earth System Model ensemble.*

[14] Hátún, H., Sandø, A. B., Drange, H., Hansen, B., & Valdimarsson, H. (2005). Influence of the Atlantic subpolar gyre on the thermohaline circulation. *Science*, 309(5742), 1841-1844.

[15] Holliday, N. P., Meyer, A., Bacon, S., Alderson, S. G., & de Cuevas, B. (2007). Retroflection of part of the east Greenland current at Cape Farewell. *Geophysical Research Letters*, 34(7).

[16] Katsman, C. A., Spall, M. A., & Pickart, R. S. (2004). Boundary current eddies and their role in the restratification of the Labrador Sea. *Journal of Physical Oceanography*, 34(9), 1967-1983.

[17] Lavender, K. L., Davis, R. E., & Owens, W. B. (2000). Mid-depth recirculation observed in the interior Labrador and Irminger seas by direct velocity measurements. *Nature*, 407(6800), 66-69.

[18] Lazier, J., Hendry, R., Clarke, A., Yashayaev, I., & Rhines, P. (2002). Convection and restratification in the Labrador Sea, 1990–2000. *Deep Sea Research Part I: Oceanographic Research Papers*, 49(10), 1819-1835.

[19] Lherminier, P., Mercier, H., Huck, T., Gourcuff, C., Perez, F. F., Morin, P. & Falina, A. (2010). The Atlantic Meridional Overturning Circulation and the subpolar gyre observed at the A25-OVIDE section in June 2002 and 2004. *Deep Sea Research Part I: Oceanographic Research Papers*, 57(11), 1374-1391.

[20] MATLAB and Statistics Toolbox Release 2016b, The MathWorks, Inc., Natick, Massachusetts, United States.

[21] Marzocchi, A., Hirschi, J. J. M., Holliday, N. P., Cunningham, S. A., Blaker, A. T., & Coward, A. C. (2015). The North Atlantic subpolar circulation in an eddy-resolving global ocean model. *Journal of Marine Systems*, 142, 126-143.

[22] McDougall T. J. & Barker. P. M. (2011). Getting started with TEOS-10 and the Gibbs Seawater (GSW) Oceanographic Toolbox, 28pp., SCOR/IAPSO WG127, ISBN 978-0-646-55621-5.

[23] Pickart, R. S., Straneo, F., & Moore, G. W. K. (2003). Is Labrador sea water formed in the Irminger basin?. *Deep Sea Research Part I: Oceanographic Research Papers*, 50(1), 23-52.

[24] Pickart, R. S., Spall, M. A., Ribergaard, M. H., Moore, G. W. K., & Milliff, R. F. (2003). Deep convection in the Irminger Sea forced by the Greenland tip jet. *Nature*, 424(6945), 152-156.

[25] Pickart, R. S., Torres, D. J., & Fratantoni, P. S. (2005). The East Greenland Spill Jet. *Journal of Physical Oceanography*, 35(6), 1037-1053.

[26] Rogers, J. C. (1990). Patterns of low-frequency monthly sea level pressure variability (1899-1986) and associated wave cyclone frequencies. *Journal of Climate*, 3(12), 1364-1379.

[27] Sarafanov, A., Falina, A., Mercier, H., Sokov, A., Lherminier, P., Gourcuff, C., & Daniault, N. (2012). Mean full-depth summer circulation and transports at the northern periphery of the Atlantic Ocean in the 2000s. *Journal of Geophysical Research: Oceans*, 117(C1).

[28] Thomson, D. J. (1982). Spectrum estimation and harmonic analysis. *Proceedings of the IEEE*, 70(9), 1055-1096.

[29] Våge, K., Pickart, R. S., Sarafanov, A., Knutsen, Ø., Mercier, H., Lherminier, P., & Bacon, S. (2011). The Irminger Gyre: Circulation, convection, and interannual variability. *Deep Sea Research Part I: Oceanographic Research Papers*, 58(5), 590-614.

[30] Yashayaev, I. (2007). Hydrographic changes in the Labrador Sea, 1960–2005. *Progress in Oceanography*, 73(3), 242-276.

Appendix: Extra figures

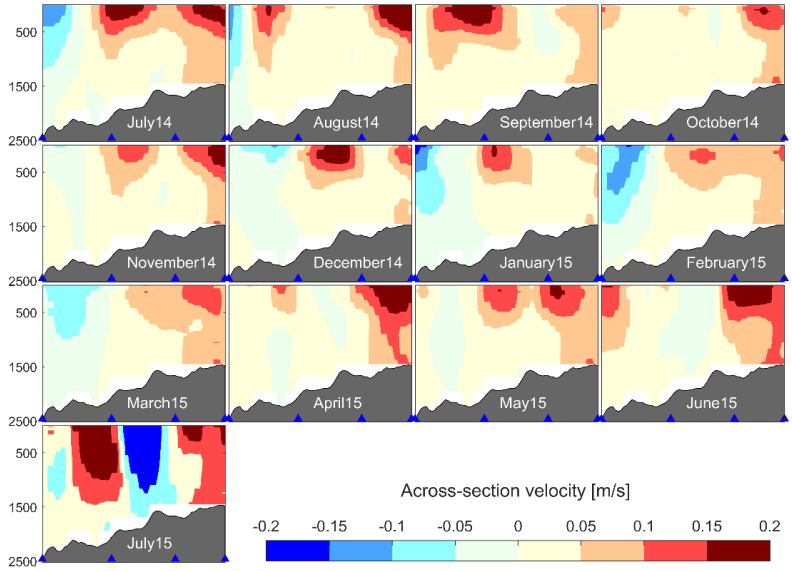

FIGURE 32: Monthly mean across-section velocities in the section from the model output. Positive/negative values indicate northward/southward flow.

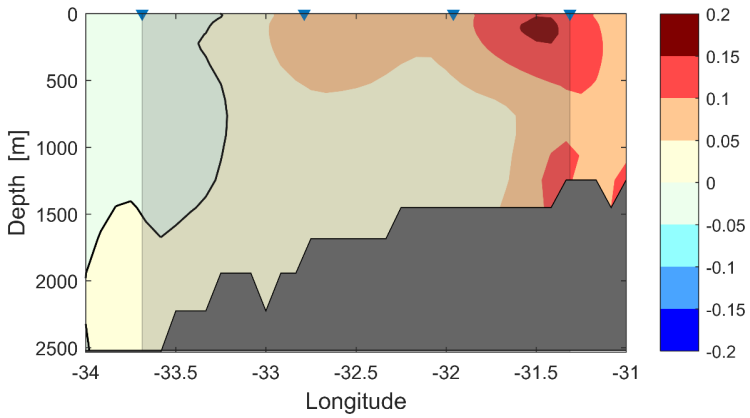

FIGURE 33: Yearly mean across-section velocity field from the model output. Positive/negative values indicate northward/southward flow. Downward looking triangles indicate the location of the moorings. From west to east: IC_1, IC_2, IC_3, IC_4.

Music from time series

Nika Pasuri is an electronic music composer who was inspired by this study and used the time series of the volume transport of the Irminger Current to compose two songs. These songs are freely available online through the following link:
https://soundcloud.com/nikapasuri/sets/transport-and-variability-of